Future socio-ecosystem productivity threatened by compound drought-heatwave events

Jiabo Yin[1*], *Pierre Gentine*[2,3], *Louise Slater*[4], *Lei Gu*[5], *Yadu Pokhrel*[6], *Naota Hanasaki*[7], *Shenglian Guo*[1], *Lihua Xiong*[1], *Wolfram Schlenker*[8]

[1] State Key Laboratory of Water *Resources* and Hydropower Engineering Science, Wuhan University, Wuhan 430072, China

[2] Department of Earth and Environmental Engineering, Columbia University, New York, NY 10027, USA

[3] Earth Institute, Columbia University, New York, NY 10025, USA

[4] School of Geography and the Environment, University of Oxford, Oxford, UK

[5] School of Civil and Hydraulic Engineering, Huazhong University of Science and Technology, Wuhan 430074, China

[6] Department of Civil and Environmental Engineering, Michigan State University, East Lansing, MI, USA

[7] Center for Climate Change Adaptation, National Institute for Environmental Studies, Tsukuba, Japan

[8] School of International and Public Affairs, Columbia University, New York, NY 10027, USA

*Correspondence: J. Yin –jboyn@whu.edu.cn

Abstract

Compound drought-heatwave (CDHW) events are one of the worst climatic stressors for global sustainable development. However, the physical mechanisms behind CDHW and their impacts on socio-ecosystem productivity remain poorly understood. Here, using simulations from a large climate-hydrology model ensemble of 111 members, we demonstrate that the frequency of extreme CDHWs is projected to increase by ten-fold globally under the highest emissions scenario, along with a disproportionate negative impact on vegetation and socioeconomic productivity by the late 21st century. By combining satellite observations, field measurements and reanalysis, we show that terrestrial water storage and temperature are negatively coupled, likely driven by similar atmospheric conditions (e.g., water vapor deficit and energy demand). Limits on water availability are likely to play a more important role in constraining the terrestrial carbon sink than temperature extremes, and over 90% of the global population and GDP could be exposed to increasing CDHW risks in the future, with more severe impacts in poorer or rural areas. Our results provide crucial insights towards assessing and mitigating adverse effects of compound hazards on ecosystems and human well-being.

Main text

Drought and heatwaves are driven by complex interactions between physical processes and often initiated by similar synoptic circulation anomalies[1-2], and are thus likely to occur simultaneously[3-4]. As droughts are occurring more frequently and atmospheric warming triggers stronger land-atmosphere feedback, the risks of compound drought-heatwave (CDHW) events are intensified across the globe[5-6], amplifying adverse impacts on socioeconomic sustainability and human well-being[7-8]. CDHW can for example exacerbate vegetation mortality, which, in turn, may cascade into other hazards, such as wildfires and crop yield losses[9-11]; they can also jeopardize electric grid reliability and adversely affect a wide range of natural and human-made systems[12]. In the U.S. alone, three CDHWs between 2011 and 2013 caused economic damages of roughly $60 billion[6].

How CDHWs regulate ecosystem productivity is also an important issue. The terrestrial biosphere acts as a prominent sink for anthropogenic CO_2, sequestering about 30% of annual CO_2 emissions[13-14]. However, climatic extremes can adversely affect its ability to function as a sink; for example, the 2003 European drought and heatwave reduced plant productivity by ~30%, thereby cancelling four years of CO_2 net uptake over Europe[15]. After severe CDHWs, plant recovery usually lags owing to reduced growth, non-reversible losses in hydraulic conductance or depletion of carbon reserves[16-17]. This lagged growth may in turn increase vulnerability to another CDHW if it occurs before complete recovery[8], potentially limiting the capacity of continents to act as a carbon sink[18-19].

With growing evidence about these damages, CDHWs are increasingly regarded as one of the worst climatic stressors to global socioeconomic sustainability and ecosystem health[20-22]. Understanding CDHW dynamics in a warming Earth is thus essential for the implementation of the UN Sustainable Development Goals (SDGs), in particular SDG13 that aims to combat climate change and its impacts. Yet, how to describe CDHW remains an open question, particularly in terms of defining a fully representative stress index[23]. Previous studies have assessed droughts through a variety of indices such as the (self-calibrated) Palmer Drought Severity Index (PDSI) and the soil moisture (SM) drought index[24]. More recently, terrestrial water storage (TWS), a key determinant of global water and energy budgets, has been employed to reveal large-scale drought impacts on hydrologic systems and plant growth. TWS represents the vertically integrated water storage as opposed to conventional indices that only capture partial water storages or fluxes[25-26]. However, the effects of TWS on future shifts in

CDHW dynamics and the resulting impacts on socio-ecosystem productivity remain unexamined.

Here, we present a quantitative assessment of the socioeconomic and ecological consequences of CDHWs at a global scale, under both current and future climates. We first analyse the association between daily maximum near-surface temperature (T_{max}) and TWS from satellite observations, field measurements, Gravity Recovery and Climate Experiment (GRACE)-constrained reconstruction and reanalysis data during 1979-2020. We detect strong multi-temporal-scale coupling during the warm season (Supplementary Fig. 1), highlighting the high likelihood of concurrent drought and heat extremes. To assess the physical mechanisms behind CDHW, we measure the responses of large- and local- scale atmospheric dynamics to heat stress, drought and their temporally compounding extremes. We then evaluate the effects of climatic extremes on the terrestrial carbon budget by using net ecosystem productivity (NEP) as well as its partitioning into photosynthesis (i.e., GPP) and respiration (i.e., total ecosystem respiration, TER). We do this by employing *in situ* eddy-covariance flux tower observations, a recent satellite-based machine-learning-generated solar-induced chlorophyll fluorescence (SIF) dataset[27], and a light use efficiency theory-based GPP dataset[28]. Moreover, we assess future shifts in CDHWs for various socioeconomic and ecological subgroups using a large ensemble (96 scenarios) of climate-hydrology simulations under the Inter-Sectoral Impact Model Intercomparison Project phase 2b (ISIMIP2b; Supplementary Table 1), and 15 members of TWS simulations by driving the H08 global hydrological model with bias-corrected Coupled Model Intercomparison Project Phase 6 (CMIP6) ensemble outputs. Finally, we examine the changes in joint return period (JRP) using a "AND" hazard scenario of CDHWs under a bivariate non-stationary framework, and systematically quantify the associated uncertainty (more details in the Methods).

Results

Observed water-heat-carbon dynamics in climatic extremes

Land-water-content indicators (i.e., TWS and SM) and T_{max} are negatively correlated globally (Fig. 1i and Extended Data Fig. 1), likely due to the increase in evapotranspiration during the warm season. The bimodality, i.e., the binning distribution toward both ends, suggest that extreme stressors should not be assessed in isolation (Extended Data Fig. 1e-h), and can be explained by land-atmosphere coupling[29]. To disentangle the influence of atmospheric conditions on climatic extremes, we estimate the anomalies of composite variables during drought events, heat extremes and concurring CDHW events. Heat extremes (above the 90th percentile of T_{max}) occur under large-scale atmospheric conditions such as high convective available potential energy (CAPE) and high convective inhibition (CIN) co-occurring in higher-latitude regions (Fig. 1 a-b). High CAPE suggests a high moist convection potential, thereby enhancing the likelihood of intense rainstorms. The moist convection potential over land is also linked to higher sensible heat flux, latent heat flux (upward positive) and column-integrated water vapour (CIWV), correlated with higher specific humidity (SH) over most lands in the Northern Hemisphere (Fig. 1 c-f). Nevertheless, atmospheric moisture transport has weakened across almost the entire global land surface, as indicated by widespread negative anomalies of vertically integrated moisture convergence (VIMC), and thus decreases relative humidity (RH) over land (Fig. 1 g-h). In the tropics and in several regions of the mid-latitudes, low CAPE is accompanied by high CIN and weak water-heat transport strength (negative anomalies of latent heat flux, CIWV, SH, VIMC and RH), which may enhance air dryness and thus propagate into terrestrial droughts (Fig. 1 a-h). At higher latitudes and in dry conditions (as identified by a TWS-based Drought Severity Index, TWS-DSI < -0.8, more details in the Methods), we detect negative anomalies of CAPE, CIWV, SH and latent heat flux, which is opposite to the patterns found during extreme heat conditions (Supplementary Fig. 2). In the remaining land regions, the pattern of anomalies of water-heat variables are largely consistent with heat conditions, even though their responses to dry events are weaker than the responses to heat extremes. Due to these regionally divergent impacts of heat and dry extremes, the atmospheric conditions during concurrent heat-dry conditions generally indicate a more severe air dryness as well as less moist convection and water vapour transport, particularly in the mid-latitudes and tropics (Supplementary Fig. 3).

We then evaluate the impacts of these climatic extremes on the terrestrial carbon budget at global eddy-covariance tower sites (Supplementary Fig. 4; Supplementary Table 2). We find a strong negative correlation between observed T_{max} and daily GLADS-based TWS ($r = -0.2$, $p<0.001$) (Fig. 1n), along with a bimodal behaviour (Fig. 1j). GPP responds to T_{max} both nonlinearly and nonmonotonically: at low T_{max}, GPP is enhanced with rising T_{max} as it promotes photochemistry by warming[30-31]; however, when T_{max} is very high, further increases in T_{max} cause GPP stress (Fig. 1k), which strongly inhibits plant photosynthesis[32]. TER increases with T_{max}, yet at a more moderate pace than GPP (Fig. 1l), so that net ecosystem exchange still responds negatively to the highest T_{max} (Fig. 1m). TWS depletion might reduce GPP and TER, as water stress reduces photosynthesis through stomatal and non-stomatal regulation and respiration through soil enzyme activities. Under concurrent high T_{max} and low TWS, NEP mean anomalies (-1.42 $gCm^{-2}day^{-1}$) are largely determined by GPP anomalies (-1.25 $gCm^{-2}day^{-1}$), while TER is slightly increased with mean anomaly of 0.30 $gCm^{-2}day^{-1}$ (Fig. 1o). When assessing these same relationships using *in situ* root-zone SM as well as monthly TWS from three GRACE/GRACE-FO solutions, we still detect impairing effects of heat and dry extremes on terrestrial carbon uptake (Extended Data Fig. 2). The machine-learning-generated SIF and MODIS-retrieved GPP anomalies are negative in most regions during extreme heat, drought and concurrent extremes (Extended Data Fig. 3), except in boreal regions and small areas of tropical rainforests such as the Amazon forests, where SIF and GPP are enhanced because ecosystems tend to be temperature limited[29,33]. The potential for heat or dryness carbon loss therefore needs to be understood when exploring the impacts of concurrent extreme climatic events on ecosystems.

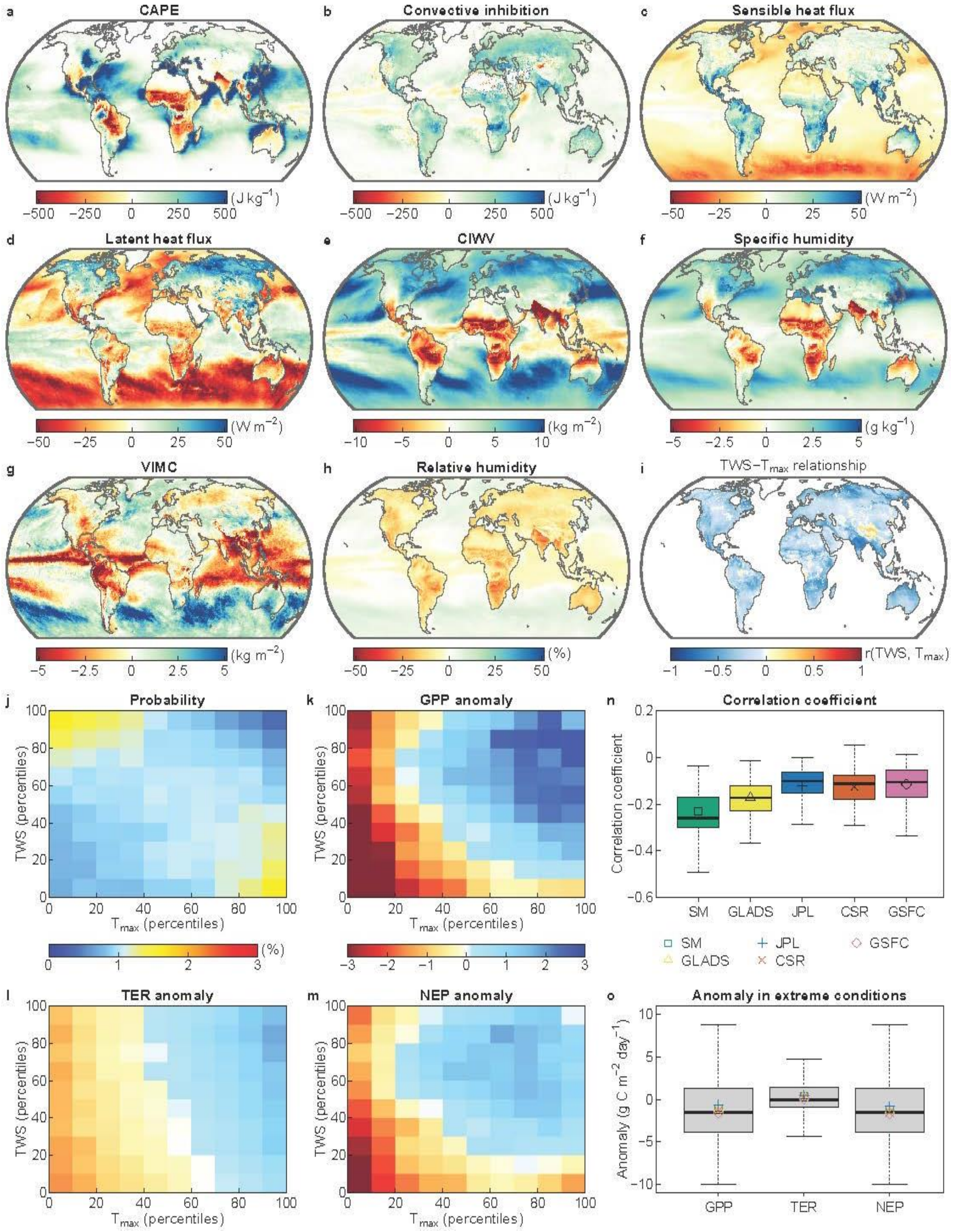

Fig. 1 | Anomalies of composite water-heat-carbon variables during extreme climatic events. a-h, Anomalies of CAPE (**a**), convective inhibition (**b**), sensible heat flux (**c**), latent heat flux (**d**), CIWV (**e**), specific humidity (**f**), VIMC (**g**) and relative humidity (**h**) during extreme heat events. The extreme heat events in **a-h** are identified using the 90th percentile of ERA5 T_{max} in each grid cell. **i**, Pearson's correlation coefficient between daily GLADS TWS and ERA5 T_{max}. **j**, Mean probability of each percentile bin of T_{max} and daily GLADS TWS across 73 flux tower sites. **k-m**, Mean anomalies of GPP (**k**), TER (**l**), and NEP (**m**) for each percentile bin of T_{max} and GLADS TWS across 73 flux tower sites. **n**, Pearson's correlation coefficient between T_{max} and TWS (or SM) from different dataset across 73 flux tower sites. **o**, Anomalies of GPP, TER, and NEP above 90th percentiles of T_{max} and below 10th percentiles of daily TWS (or SM) across 73 flux tower sites. **k-m** share the same colorbar and the unit is g C m^{-2} day^{-1}. The daily TWS in **j-m** and the boxplot in **o** are from the GLADS-2.2 dataset. In **n-o**, mean values of different datasets are marked by different shapes, and the centre line indicates median value; the box bounds (whiskers) indicate 25th/75th percentile (min/max) values. At each site/grid, anomalies of the variables are calculated as the difference between the daily values in extreme events and the mean daily values in the 5-month warm season.

Observed increases in climatic extremes and their impacts

Recent changes in climatic extremes are evaluated in terms of their frequency, days, duration and severity (see definitions in Methods). Globally, the frequencies of the three types of climatic extreme events (heatwave, drought and CDHW) are increasing; for example, 67% of global land areas have experienced more CDHWs in recent decades (Fig. 2a). The duration and severity of CDHW are greatly increasing in the eastern U.S., central South America, parts of central Africa, eastern Europe, the Middle East and parts of eastern Asia (Fig. 2b; Supplementary Fig. 5). Further, the global average coincidence rate (i.e., the ratio of CDHW to heatwave events, CDHWr, 2.75%/decade), exposed land area (4.94%/decade), exposed population (4.65%/decade) and exposed Gross Domestic Product (GDP, 5.24%/decade) have all significantly increased since 1979 (Fig. 2c). Eight of the Giorgi climate regions are identified as CDHW hotspots (i.e., AMZ, CAM, ENA, CNA, MED, SSA, NAS and EAS; see locations in Fig. 2f), where CDHWs have both long duration and severe magnitude (Supplementary Fig. 6). The hotspots are located in areas with high CDHWr, where heatwaves and droughts have a high likelihood to occur simultaneously, and are accompanied by stronger negative r(TWS, T_{max}) (Fig. 2d-e). Five (three) out of eight hotspots show significant (insignificant) increases in socioeconomic (either GDP or population-weighted) exposure due to exacerbated CDHWs (Extended Data Fig. 4; Supplementary Fig. 7); some regions even show increasing rates of >10%/decade for both GDP and population exposure. The three GRACE/GRACE-FO solutions detect similar hotspots to the reconstructed data (Supplementary Figs. 8-10), but indicate stronger trends and socioeconomic exposures (Supplementary Figs. 11-13), which may be driven by more rapid intensification of warming and drying in the last decade, implying that tackling and adapting to these climatic hazards is a growing societal challenge.

A comparison of the coupled TWS-DSI index with traditional drought indices suggests that TWS-DSI provides new information and a stronger signal of drought exacerbation in recent decades. Unlike the standardized runoff index (SRI), which is highly correlated with the standardized precipitation index (SPI), TWS-DSI exhibits substantial changes over time in most of the Giorgi regions (Supplementary Figs. 14-16), because it encompasses all surface and subsurface storage components that are relevant to terrestrial water availability. TWS-DSI also differs from the standardized precipitation evapotranspiration index (SPEI) and SM-based indices, which fail to characterize real conditions of soil and groundwater (surface water storage such as ice and snow) (Supplementary Figs. 17-19). The TWS-DSI index suggests that the drought magnitudes have substantially changed across most Giorgi regions in recent decades, while the other indices show negligible changes between the two periods, thus underestimating drought intensification in most sub-regions and at the global scale. This considerable difference between the ability of different indices to estimate temporal changes underscores the importance of considering groundwater and human activities in assessing drought risks[26,34], by using an integrated index such as TWS-DSI.

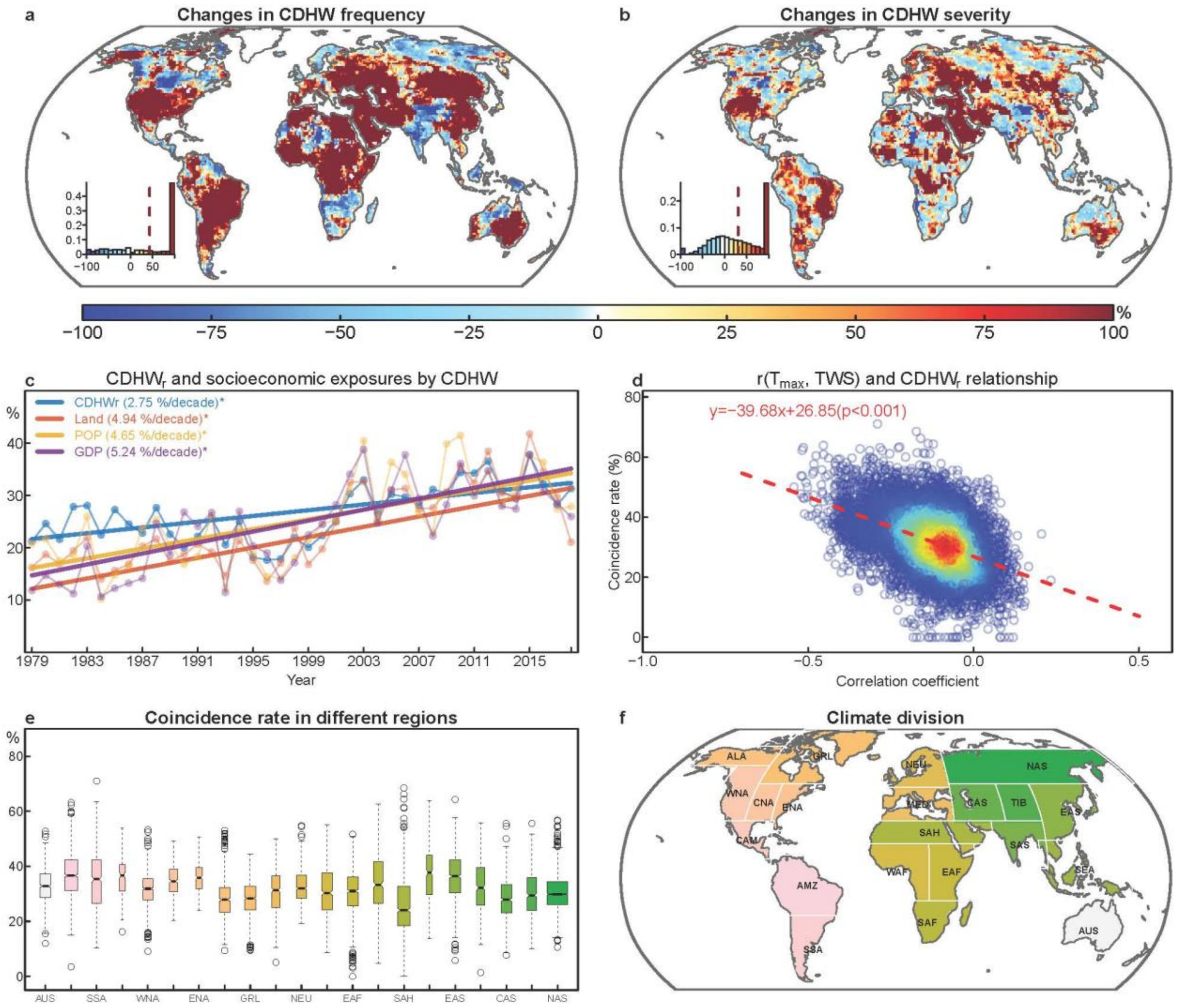

Fig. 2 | Recent changes in frequency and intensity of CDHW as well as related socioeconomic exposure. **a-b,** Changes in frequency (**a**) and severity (**b**) of CDHW between two periods (recent, 1999-2019, minus past, 1979-1998). Insets in **a-b** show the histogram of the relative change percentages, with the dashed vertical line representing the mean value. **c**, Temporal dynamics of the global average coincidence rate (CDHWr), and fraction of land area (Land), population (POP) and GDP that is exposed to CDHW. **d**, Relationship between r(T_{max}, TWS) and CDHWr across the land grids (excluding Greenland and Antarctica); the two-sided F test is use for testing significance. **e-f,** boxplots of coincidence rate (**e**) in 21 different Giorgi climate regions (**f**). For the box plots in **e**, the centre line indicates median value; the box bounds (whiskers) indicate 25th/75th percentile (min/max) values, and the outliers are presented. The droughts are identified by reconstructed TWS data, and the heatwaves are detected by using T_{max} from the Berkeley Earth Surface Temperatures (BEST) dataset. The * in **c** indicates the change is significant ($p<0.05$) detected by Mann-Kendall test.

Projections of climatic extremes and socio-ecosystem effects

Before projecting future CDHW characteristics, we first evaluate the anomalies of composite water-heat-carbon variables during extreme climatic events, under historical and future periods (Supplementary Figs. 20-22; Supplementary Text 1 and Fig. 3). RH (surface downwelling shortwave and longwave radiation) is globally decreasing (increasing) with a stronger rate during CDHWs than during individual climatic extremes. In contrast, the SH anomalies are not globally consistent and display a different sign in the tropics and other land regions (Fig. 3 a-l). Heat-extreme GPP anomalies are negative in most regions except in the water-limited boreal regions (Supplementary Fig. 20 m-o). TER is greatly enhanced in boreal regions but slightly reduced over most other regions between 50°S and 50°N, in agreement with flux tower sites (Supplementary Fig. 20 p-r; Fig. 1l), which are mostly located in the mid and low latitudes (Supplementary Fig. 4). The negative effect of extreme low TWS on GPP significantly exceeds the effect of extreme high T_{max} in future simulations over more than 80% (75%) of land areas under RCP8.5 (RCP6.0), highlighting the increasing importance of water limitation for future carbon assimilation (Supplementary Figs. 20-22 m-u). We also project the anomalies of GPP, TER and NEP using the Community Land Model (CLM 4.5) forced by bias-corrected GFDL-ESM2M climate data, and these independent evaluations corroborate the increasing constraining role of limited water availability for the future carbon sink (Extended Data Fig. 5; Supplementary Fig. 23). During concurrent heat and drought conditions, photosynthesis and respiration are both reduced, as detected by strong negative anomalies of GPP, TER and NEP in most global land areas except for the boreal high-latitudes (Fig. 3 m-u), implying large reductions in ecosystem carbon uptake in a future warmer climate.

Negative NEP anomalies under CDHWs are much stronger than when considering only one extreme, particularly under future climate (Fig. 3; Supplementary Figs. 20-23; Extended Data Fig. 5). The projected reductions in carbon uptake during compounding drought-heat events occur alongside general increases in global productivity from CO_2 fertilization[35-36]. This paradox may be explained by the fact that the CO_2 fertilization effect on GPP is offset by the increase in compound events in some regions (e.g., Amazon region and southern Europe)[19], where the respiration losses lead to lower future NEP than in historical simulations with minimal projected increases in GPP. Vegetation mortality and subsequent regrowth and succession processes are usually poorly simulated by Earth system models (ESMs). If large drops in productivity driven by extreme events lead to enhanced vegetation mortality, the effects of climatic extremes on terrestrial productivity and carbon storage may be greater than those simulated by ESMs[37].

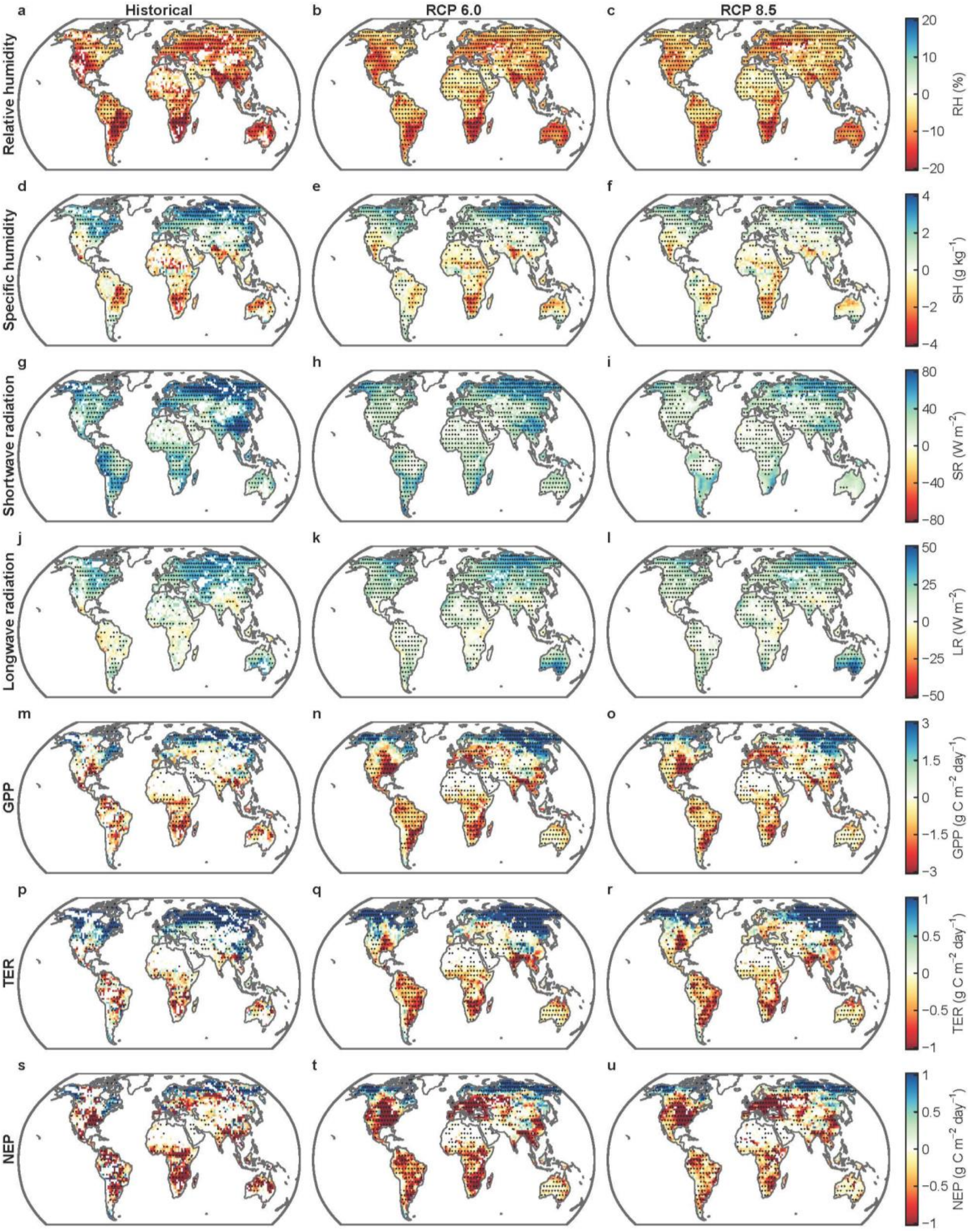

Fig. 3 | Anomalies of water, heat and carbon fluxes due to concurrent hot-drought conditions during historical and future periods by climate models. **a-l**, Anomalies of relative humidity (RH, **a-c**), specific humidity (SH, **d-f**), surface downwelling shortwave radiation (SR, **g-i**), longwave radiation (LR, **j-l**) during CDHW. **m-u**, anomalies of GPP (**m-o**), TER (**p-r**) and NEP (**s-u**) due to high monthly T_{max} (above 90th percentile) and low TWS (TWS-DSI< -0.8). Anomalies of RH, SH, SR and LR (GPP, TER and NEP) are calculated as the difference between daily (monthly) values in concurrent hot-drought conditions and the mean values during the entire warm season. Stippling denotes regions where the sign of the relative changes is consistent with the sign of multi-model means (as shown in the figure) in at least 80% of ESM-THM (terrestrial hydrological model) combinations. The historical anomalies (left column) combine historical and RCP 6.0 TWS data to estimate the TWS-DSI.

The occurrence of CDHW is projected to increase four-fold over half of the global landmasses (Fig. 4 a-c), and the number of CDHW days is projected to increase six-fold in 68% of the globe under all RCPs (Extended Data Fig. 6). Almost 70% of global land areas are projected to experience a four-fold intensification of CDHW duration and severity under the medium and high emission pathways (i.e., RCP 6.0 and RCP 8.5), while the RCP 2.6 suggests a weaker (i.e., two-fold) intensification rate (Fig. 4 d-f; Extended Data Fig. 6). Generally, the intensification is greatest for CDHW, followed by heatwaves, then droughts, which suggests that heatwaves may play a dominant role in exacerbating future CDHW (Fig. 4; Extended Data Fig. 6; Supplementary Fig. 24). The increased $CDHW_r$ indicates that the interdependence between heatwave and droughts is growing as the climate warms (Fig. 4g). The fraction of the global land area, population and GDP exposed to CDHW are generally projected to increase until the late 21st century (Fig. 4h-j). Under RCP 2.6, the global land area exposed to CDHW increases from 18% during the baseline period to 34% by end of the 21st century, while the exposed global fraction of population and GDP increases from 19% and 18%, respectively to ~36% each by 2070s, and then slightly decreases to 31% and 30%, respectively, by end of this century. Under RCP 6.0 (RCP 8.5), substantial increases are projected in CDHW exposure, global fractional land area, population exposure and GDP exposure, from ~17% (16%) during the baseline period to 40%, 38% and 41% (38%, 36% and 36%), respectively. Overall, an additional 17-21% (18-25%) of the global population (GDP) is projected to be exposed to CDHW in future climates, which translates to an additional ~1.4 billion to ~1.7 billion people (~13 trillion to ~20 trillion U.S. dollars at 2015 PPP (purchasing power parity)) per year. With TWS simulated by the H08 model forced by five bias-corrected CMIP6 models under three shared socioeconomic pathways (SSPs) (see details in Methods), we find stronger exacerbation of CDHW and associated socioeconomic exposure than the CMIP5-oriented projections, accompanied by a reduced uncertainty (Extended Data Fig. 7; Supplementary Fig. 25).

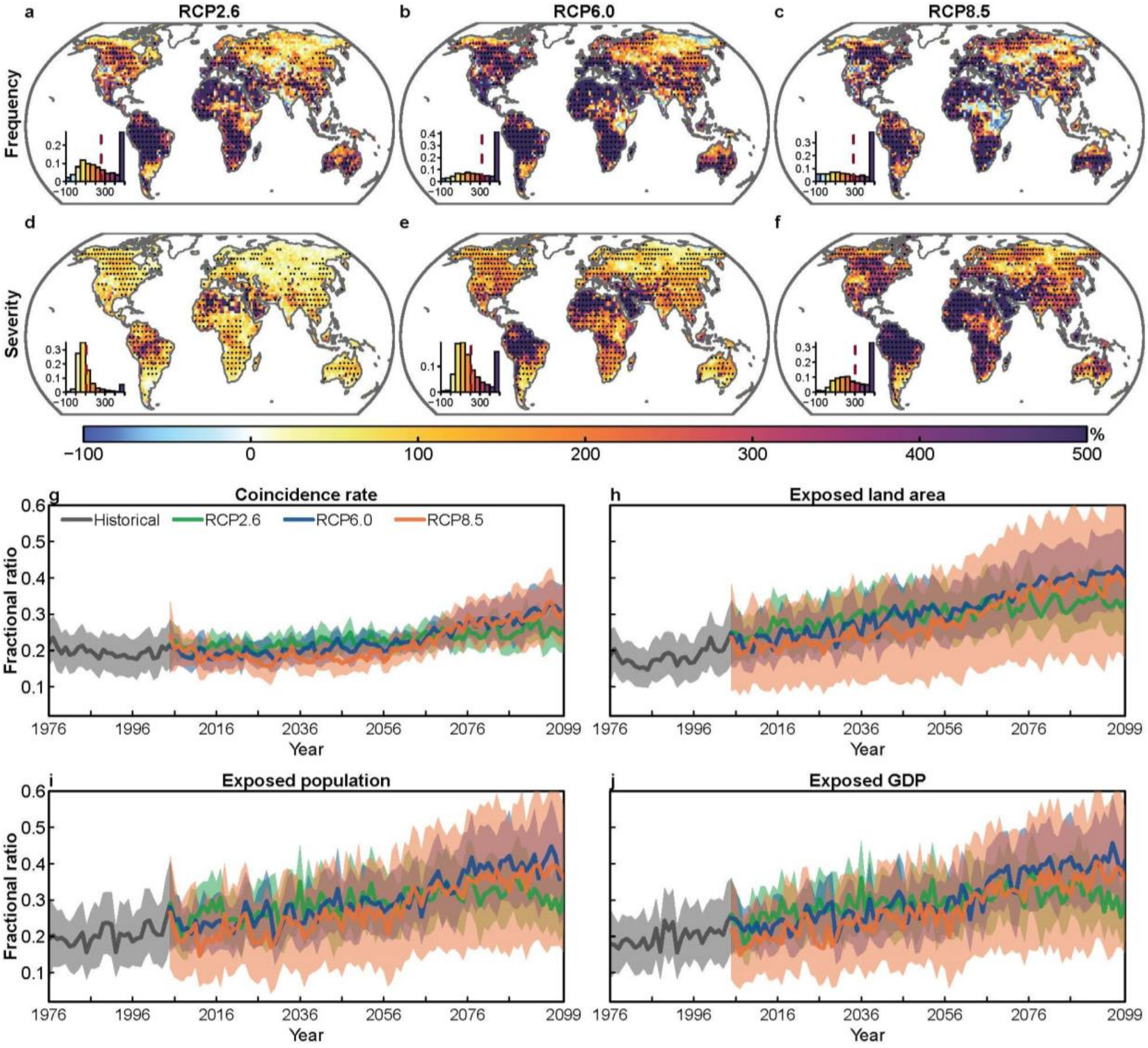

Fig. 4 | Future changes in the characteristics of CDHW and socioeconomic exposure to CDHW under model simulations. a-f, Relative changes in the frequency (**a-c**) and severity (**d-f**) of CDHW from the historical to future periods. **g-j**, Temporal dynamics of the global average coincidence rate (**g**), exposed land area (**h**), exposed population (**i**) and exposed GDP (**j**). Insets in **a-f** show the histogram of the relative change percentages, with the dashed vertical line representing the mean value. Stippling in **a-f** denotes regions where the sign of the relative changes is consistent with the sign of the multi-model means (as shown in the figure) in at least 80% of GCM-THM models. In **g-j**, the shading represents ±1 standard deviation (SD), and the historical exposures are presented only by combining historical and RCP 2.6 TWS data in estimating the TWS-DSI. These results are derived from the ISIMIP2b multiple impacts model ensemble.

Future bivariate risks of CDHW and associated uncertainty

Under RCP8.5 (or RCP2.6, RCP6.0), the JRPs of the historical 50-year CDHW (as measured during the period 1976-2005) are projected to be below 10 years in more than 85% (or 52%, 75%) of global land areas. We find high inter-model agreement, implying that the occurrence of CDHW extremes will be at least five-fold globally by the end of this century (Fig. 5d; Supplementary Fig. 26a-c). Most hotspots might even experience a ten-fold intensification of CDHW occurrence by end of the century, as the historical 50-year CDHW is projected to occur once every five years by then under RCP8.5. Similarly, the three RCP scenarios project that over 90% of the population and GDP in most global land areas will be exposed to increasing CDHW risks by the end of this century (Supplementary Fig. 26d-i). Moreover, the exposed land area, population, and fraction of global GDP are all increasing as the climate warms, with the global average fraction of land area exposed to the historical 50-year CDHW increasing from about 82% to nearly 100% by end of this century (Fig. 5 a-c). The CMIP6-based ensemble simulations from H08 indicate even higher bivariate risks of CDHW, as the fraction of population and GDP that is exposed might approach 100% with smaller uncertainty by 2100, and the average JRP of the historical 50-year CDHW is projected to be below the 5-year return period across almost all the climate regions under SSP585, suggesting a ten-fold intensification (Extended Data Fig. 8a-m).

Last, we decompose the overall uncertainty into different components of seven (three) different sources for CMIP5- (CMIP6-) based projections at the global scale by using the multivariate analysis of variance (ANOVA) method (Methods). The uncertainty contribution ratios vary across different regions, due to the different RCPs and THMs (Supplementary Fig. 26j-p; Extended Data Fig. 8n). For example, in the Amazon forests, the RCPs and THMs induce ~27% and 22% of the overall uncertainty, respectively. The interaction between scenarios, GCMs and THMs also plays an important role (Fig. 5e), and reveals the importance of examining CDHW changes by using a large climate-scenario ensemble and exploring the interaction of different models for projecting future climatic extremes.

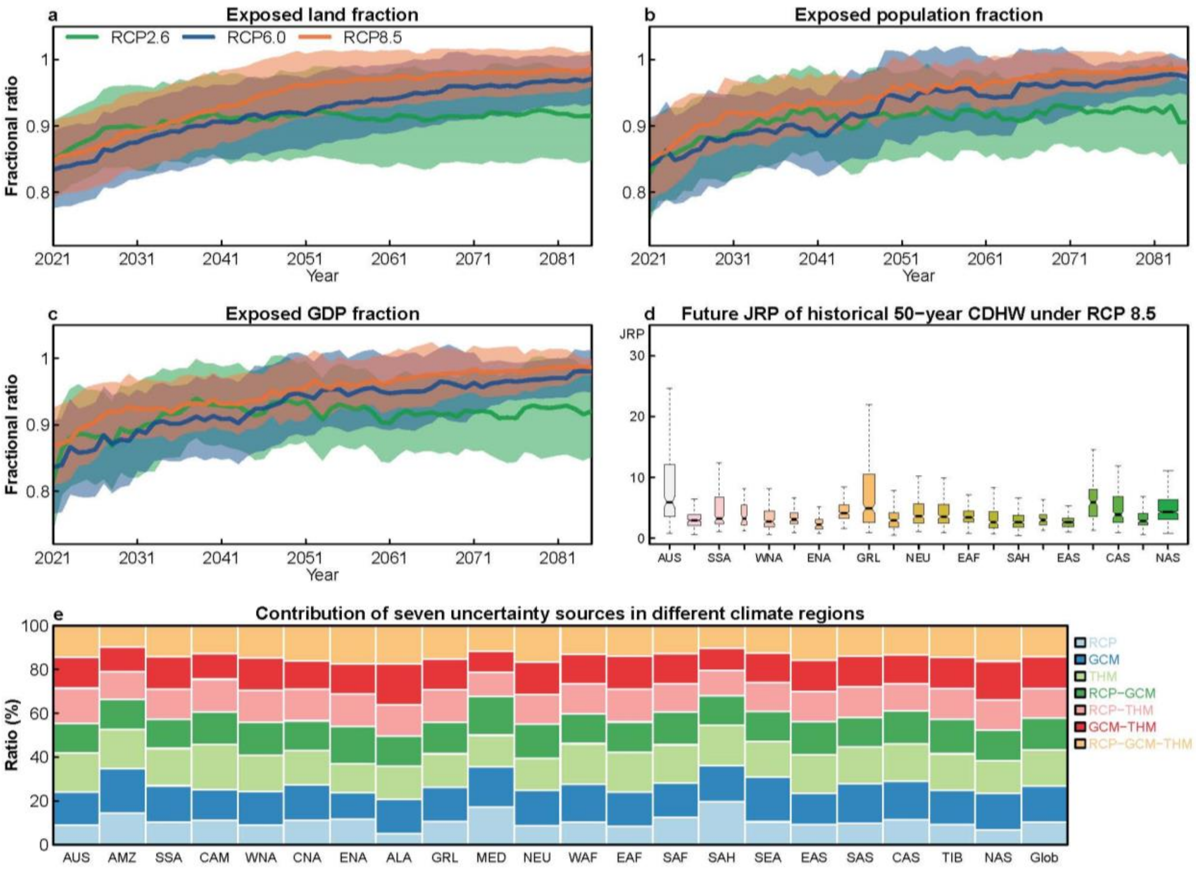

Fig. 5 | Projected JRP of historical 50-year bivariate CDHW and socioeconomic exposure. a-c, Temporal dynamics of the fraction of global average exposed land area (**a**), population (**b**) and GDP (**c**) due to increasing CDHW risk; the solid curve and shading indicate multi-model mean ±SD. **d**, Boxplot of updated JRP of the historical 50-year CDHW in different Giorgi climate regions under RCP 8.5; the centre line indicates median value, and the box bounds (whiskers) indicate 25th/75th percentile (min/max) values. **e**, Average contribution ratios of seven uncertainty sources in different Giorgi climate regions and the global landmass (Glob). These results are derived from the ISIMIP2b multiple impacts model ensemble.

Discussion

Large-scale atmospheric anomalies (blocking, subsidence, and free tropospheric warming) play a key role in the coupling of T_{max} and TWS, and have been recognized as important drivers of the onset and development of droughts and heatwaves[38-40]. The strong coupling of T_{max} and TWS suggests that the impacts of associated extremes (i.e., heatwave and droughts) should not be assessed in isolation. Compound droughts and heat extremes reduce terrestrial carbon uptake much more strongly than either of the two in isolation. The decline in carbon uptake induced by compound extreme events could be partially offset by CO_2 fertilization effects in the future[19], but this offset does not occur in most regions in the projections by models. Climate models project increases in the negative effects of compound extreme events on NEP such that, despite CO_2 fertilization effects, future NEP during compound extreme events remains unchanged or decreases slightly in reference with historical conditions, especially in the Amazon and southern Europe. Our large climate-hydrology model ensemble under both CMIP5/6 projects that CDHW magnitudes (occurrence, duration and severity) will quadruple in 70% of global land areas under medium and high emission scenarios. The $CDHW_r$ is also increasing globally, indicating that the interdependence between heatwave and droughts is strengthening as the climate warms. Importantly, we find that the frequency of extreme CDHW (historical 50-year event) will increase ten-fold under the highest emission scenario, and over 90% of the world population and GDP is projected to be exposed to increasing bivariate CDHW risks in the future climate under all SSPs/RCPs.

As poor people often live in risky areas and have limited capacity to adapt, they might be more exposed or more vulnerable to natural disasters than wealthier people[41-42]. Numerous studies have reported that climate change might have unequal impacts on people with different levels of annual income[43-44]. We therefore examine whether the CDHW risks and corresponding socioeconomic exposure are different between poorer and richer subgroups (refer to Supplementary Text 2 for identification). Focusing on the bottom and top quintile, i.e., grid cells where GDP per capita is below the 20th percentile or above the 80th percentile in each climate region, we find that the poorer areas have a higher fraction of the population and GDP (0.44 and 0.44, respectively) exposed to CDHW than the richer areas (0.39 and 0.38, respectively) by 2070-2099 under SSP585 (Extended Data Fig. 9). Poorer people in most Giorgi regions (e.g., AUS, EAS and TIB) are more vulnerable to CDHW than wealthy people in terms of higher $CHDW_r$ and socioeconomic exposure. These disproportionate effects are not found in a few other regions (e.g., AMZ and NEU), suggesting that regional complexity should be considered when designing climate mitigation policies. Similarly, people in urban areas are generally more capable of adapting, mitigating, and insulating themselves and their livelihoods from the effects of CDHW, relative to rural populations. Therefore, we also compare the CDHW risks in rural versus urban areas, which are defined by using the bottom and top quintile of population density in each region (Supplementary Text 2). Rural areas are projected to face higher $CDHW_r$ and GDP and population exposures than urban areas under climate change across all SSPs (Supplementary Fig. 27). When the rural/urban (or poor/rich) areas are defined by using a more extreme threshold (i.e., $10^{th}/90^{th}$ percentile value), we find even more disproportionate effects of CDHW (Supplementary Figs. 28-29), suggesting that poorer people currently live in marginal areas that are more exposed to extreme climatic conditions. We should note that our analysis keeps the definition of bottom quintile for GDP per capita and population density fixed at the 2015-year level, and therefore does not consider human migration or regional GDP changes. The distribution of poor and rural regions might shift under climate change (Extended Data Fig. 10; Supplementary Fig. 30), and the ultimate societal impact of CDHW is a function of the exposure and vulnerability of various groups. In future works, human management and vulnerability should be considered in different regions to understand the impacts of CDHW on socioeconomic systems. Nevertheless, our findings provide a firm conclusion that future CDHW hazards are projected to intensify significantly and challenge the sustainable development of future socio-ecosystem system. This work thus calls for stark mitigation and adaptation actions to reduce the adverse impacts of warming on societies and to sustain ecosystem productivity, easing the growing pressures on global sustainable development, particularly for poorer and rural areas in the Anthropocene.

Methods

Models, simulation settings and forcing data. The large ensemble simulations include 96 scenario-model combinations from CMIP5 and 15 combinations from CMIP6. The CMIP5-based projections include three emission scenarios (i.e., RCPs 2.6, 6.0, and 8.5), four GCMs, and eight Terrestrial Hydrological Models (THMs). The eight THMs include six global hydrological models (GHMs): CWatM, H08, MPI-HM, PCR-GLOBWB, WaterGAP2 and WaterGAP2-2c; one global land surface model (LSM): CLM4.5; and one dynamic global vegetation model (DGVM): LPJmL. All models simulate the key terrestrial hydrological (for example, soil, vegetation and river) processes (see details in Supplementary Table 3), which are forced by the ISIMIP2b daily meteorological forcing data[45] from four GCMs under the CMIP5 (Supplementary Table 1). For each GCM, we use both bias-corrected outputs and the TWS simulations from eight THMs, which cover both the historical baseline (1976-2005) and the future projections (2006-2099). To improve robustness of future projections, we also use TWS simulated by H08 model forced by outputs from five CMIP6 GCMs (i.e., M6A-LR, GFDL-ESM4, MPI-ESM1-2-HR, MRI-ESM2-0, and UKESM1-0-LL) under three SSPs (SSP126, SSP370, SSP585), which have been systematically bias-corrected under ISIMIP3b[46]. To assess projected impacts of climatic extremes on ecosystem productivity, we also use the GPP, autotrophic respiration and heterotrophic respiration outputs from the CLM4.5 model under historical and two RCPs (RCP 2.6 and RCP 6.0), which is forced by bias-corrected GFDL-ESM2M outputs. We deduce the TER by summing autotrophic respiration and heterotrophic respiration, and then calculate the NEP by subtracting TER from the GPP. In addition, we also use the GPP, TER and NEP of the outputs from GFDL-ESM2M, HadGEM2-ES, IPSL-CM5A-LR (not available in MIROC5). All simulations are conducted at 0.5° × 0.5° spatial resolution, but the results are bilinearly interpolate to a spatial resolution of 2°×2° for a robust projection. In each model grid cell, we define the warm season as the 5-month period with the highest mean T_{max} in the historical period.

GRACE/GRACE-FO and reconstructed TWS datasets. TWS anomalies from GRACE/GRACE-FO satellite measurements are used to evaluate global terrestrial droughts for the 2002-2020 period. We use the latest mascon products from three processing centers: the Jet Propulsion Laboratory (JPL) of California Institute of Technology, the Center for Space Research (CSR) at the University of Texas at Austin, and the NASA's Goddard Space Flight Center (GSFC). To consider possible uncertainty sourced from different processing procedures, we use the GRACE/GRACE-FO ensemble mean TWS anomalies by calculating the average time series of the three mascon datasets. To provide a long-term evaluation of climatic extremes, we also use observation-constrained monthly TWS data with a resolution of 0.5°×0.5° covering 1979-2019, which is constructed by training a statistical model with multi-source satellite and reanalysis datasets[47]. Based on two different GRACE products and three different meteorological forcing datasets, this reconstructed dataset consists of six reconstructed products of 100 ensemble members each, which has been well validated over 90 large (>500000 km^2) river basins and annual streamflow series from 12496 small (<10000 km^2) basins. We average all six products to develop an ensemble mean reconstructed TWS. To assess different drought indices, we also use the global 0.5°×0.5° SPEI data during 2002-2020 from the Climatic Research Unit (CRU) v2.6. In addition, we use the daily 0.25°×0.25° TWS data during 2003-2020 from the Catchment land surface model (CLSM) simulation under the Global Land Data Assimilation System (GLDAS-2.2).

Reanalysis and GLEAM data. We use the hourly CAPE, CIN, CIWV, surface sensible heat flux, latent heat flux, 2 m air temperature (T_{2m}), 2 m dew point temperature (T_{dew}) and air pressure (*pr*) from the fifth-generation atmospheric reanalysis of the European Centre for Medium-Range Weather Forecasts (ERA5, 1979-2020). First, the 2 m hourly RH is computed based on T_{2m} and T_{dew}, and the 2 m SH is derived by T_{dew} and *pr*. Then, we derive the daily maximum near-surface temperature (T_{max}) and daily average values of the other variables. We also use the global gridded T_{max} data during 1979-2019 from the Berkeley Earth Surface Temperatures (BEST), which incorporates approximately 39000 land stations. To identify the droughts by different indices, we use the monthly root-zone (0-100 cm) SM, precipitation and runoff from ERA5. We also use the daily root-zone SM during 1980-2020 from the GLEAM version 3.5a. In the observational analysis, the results of all different gridded datasets are bilinearly interpolated to a spatial resolution of 1°×1°. We only evaluate climatic extremes in the warm season because heat-related morbidity and mortality in the summer tend to exert the more severe impacts on socio-ecosystems. Therefore, we define the warm season as the hottest five months of the climatology of the ERA5 T_{max} for each grid cell (Supplementary Fig. 1).

FLUXNET2015 data. We use half-hourly temperature, SM, GPP, TER, and NEP data from the FLUXNET2015 dataset. SM is measured as volumetric soil water content (percentage) at all available depths. These data are processed following a consistent and uniform processing pipeline. We use temperature and SM that are gap-filled using the marginal distribution method[48]. NEP is obtained using a variable friction velocity (u*) threshold for each year, with references selected on the basis of model efficiency, and is partitioned into GPP and TER following the night-time partitioning method[49]. We select 73 sites (830 site years) with data covering no less than 3 years (Supplementary Table 2; Supplementary Fig. 4). Daytime half-hourly data (7:00 a.m. to 19:00 pm) in the warm season are aggregated to daily values. The warm season is defined as days when running 7-day mean temperatures are higher than 60th percentile of daily temperature for the site. We also use a machine learning-constrained SIF dataset and a MODIS-retrieved GPP dataset[27-28]. The SIF dataset is generated by training a machine learning algorithm based on daily OCO-2 SIF observations and colocation nadir BRDF-adjusted reflectance. This dataset can capture the seasonal and spatial variability of raw OCO-2 SIF at the far-red band (767 nm), which is demonstrated to strongly relate to spatiotemporal variation of GPP[27]. In this study, we use the clear-sky daily SIF during 2000-2020 with a 4-day temporal and 0.5° spatial resolution. The retrieved GPP dataset is based on an improved light use efficiency theory and is driven by satellite data from MODIS and climate data from NCEP Reanalysis II, and has moderate spatial (500m) and temporal (8-day) resolutions over the entire globe for 2000-2019[28].

Socioeconomic data. For the analysis of the global socioeconomic index affected by historical (1979-2020) climatic extremes, we use the global gridded 2015 population data from the Socioeconomic Data and Applications Center at Columbia University (SEDAC). This population data is consistent with national censuses and has been adjusted to match the 2015 Revision of the United Nation's World Population Prospects (UN WPP) country totals, which are produced at 30 arc-second (~1 km at the equator) resolution. We also use a global gridded 2015 GDP dataset at a 30 arc-sec resolution, which is produced by fully making use of all available sub-national data and the World Bank dataset[50]. To project future global exposure of populations and assets to climatic extremes, we employ a spatially explicit global dataset produced by employing population and urbanization projection model, and the Cobb-Douglas production model[51]. This dataset includes gridded population and GDP data under five SSPs, covering 2010-2100 at a spatial resolution of 0.5° × 0.5°, and has been widely used in climate change impact assessments[34]. Considering the socioeconomic challenges to mitigation by different development roads, the RCP2.6 (RCP6.0) scenario is associated with SSP1 (SSP4), while the RCP8.5 is associated with SSP5[52].

Deriving near-surface relative humidity and specific humidity. As near-surface RH and SH are not available in the ERA5 dataset, they are calculated by using $T_{2\mathrm{m}}$, T_{dew} and pressure. The Clausius-Clapeyron relationship can describe the relationship between saturation vapor pressure(e_{sat}) and temperature (T)[52]:

$$e_{sat}(T) = e_{s0} \exp\left[\frac{L_v}{R_v} \left(\frac{1}{T_0} - \frac{1}{T} \right) \right] \tag{1}$$

where $T_0 = 273.16\ \mathrm{K}$ and $e_{s0} = 611\ \mathrm{Pa}$ are integration constants; L_v and R_v refer to latent heat of vaporization (2.5×10^6 J kg^{-1}) and vapor gas constant (461 J kg^{-1} K^{-1}), respectively.

As the T_{dew} represents the temperature above which the water vapour will achieve saturation under constant water vapour content and pressure, it can be used to measure actual water vapour pressure. The RH can thus be deduced by substituting $T_{2\mathrm{m}}$ and T_{dew} into Eq. (1) as $RH = e_{sat}(T_{\mathrm{dew}}) / e_{sat}(T_{2\mathrm{m}})$.

SH refers to the ratio of the water vapour mass to the total air mass, which can be calculated by pr and T_{dew}[53]:

$$SH = 0.622 \frac{e_{sat}(T_{\mathrm{dew}})}{pr - 0.378 e_{sat}(T_{\mathrm{dew}})} \tag{2}$$

$\mathbf{T_{max}}$-TWS coupling and impacts. The $\mathrm{T_{max}}$-TWS coupling is evaluated by calculating the Pearson's correlation coefficient between them. We also sort observed $\mathrm{T_{max}}$ and daily SM (daily or monthly TWS) from the flux tower sites (GLADS or GRACE/GRACE-FO) into 10 × 10 percentile bins in each site and calculate the mean probability of each percentile bin of $\mathrm{T_{max}}$ and SM (or TWS) across the 73 sites. We calculate mean daily anomalies of GPP, TER and NEP in the 10 × 10 percentile bins to assess the observed mean responses of these variables to daily temperature and TWS (or SM), especially the responses to extreme high $\mathrm{T_{max}}$ and low

TWS (or SM). The drought extremes are determined according to TWS-DSI ≤ −0.8, and the heat extremes are identified by daily T_{max} is above its 90th percentile over the whole observation period (or historical period of model simulations). In addition, we examine the impacts of compound extremes on a variety of water and heat variables (e.g., RH, SH and CAPE). For both observations and GCMs simulations, we calculate their anomalies as the difference between the daily (monthly) values in heat extreme and CDHW (droughts) and the mean values in the warm season. As the daily carbon flux data are not typically archived for most GCMs, we assess the responses of GPP, TER and NEP to heat (measured by monthly T_{max} above its 90th percentile over historical period), droughts and the concurring conditions at a monthly scale, in historical and future simulations individually.

TWS-based Drought Severity Index. The recent proposed TWS-DSI index is used to identify terrestrial drought conditions[54]. The negative TWS-DSI means that the TWS is lower than the average level during the study period, and is used to represent drought magnitudes. The TWS-DSI is deduced as follows:

$$\text{TWS-DSI}_{i,j} = (\text{TWS}_{i,j} - \overline{\text{TWS}}_j) / \sigma_j \tag{3}$$

where $\text{TWS}_{i,j}$ refers to the TWS anomalies at year *i* and month *j*; $\overline{\text{TWS}}_j$ and σ_j denote the mean value and standard deviation (SD) of TWS anomalies at month *j*.

For GCM-THM TWS outputs, the same time-mean baseline as the GRACE/GRACE-FO dataset is determined, and thus monthly TWS anomalies during 1976-2099 are obtained after subtracting the mean values of TWS during 2004-2009. In calculating the mean and SD of TWS for any specified period, a common reference period (i.e., 1976-2099) is used to avoid potential exaggeration in estimating TWS variability and drought evolution, and for consistent comparison. The drought pattern in the historical period may differ slightly in each RCP/SSP as the TWS-DSI is derived from both historical and future TWS data. The droughts are characterized by four metrics: frequency, total number of drought events during the study period; days, defined as the total number of drought months; the commonly used drought severity (D_s); and duration, identified by the run theory[34]. The probability density functions for both the globe and different Giorgi climate regions during two periods are estimated using the non-parametric kernel density method. For the purpose of comparing different drought indices, we first fit the monthly ERA5 precipitation and runoff data, respectively, to the gamma distribution function to obtain monthly climatological distributions. Then, the cumulative probabilities are converted to standard normal deviates by inversing the respective cumulative distribution function, and thus the SPI and SRI are calculated. Besides these two indices and the CRU SPEI data, we also use both ERA5 and GLEAM SM data instead of TWS to characterize the drought conditions.

CDHW identification. A heatwave refers to a spell of at least three consecutive days with T_{max} exceeding the heat threshold, which is defined as the 90th percentile of T_{max} in the warm season over the entire study period. Besides, considering possible epidemiological significance[55], two successive heatwaves events are considered independent if separated by a minimum of two days; otherwise, they are clustered into a single event. We also assess the heatwave characteristics using four metrics: frequency, days, duration and the heatwave severity (HW_s). HW_s is estimated by summing the daily T_{max} anomalies:

$$HW_s = \sum_{d=1}^{d=D} \left(\left(\frac{T_{\max,d} - T_{25p}}{T_{75p} - T_{25p}} \right) \right) \quad ; D \geq 3 \tag{4}$$

where D indicates duration of the heatwave event; $T_{\max,d}$ is the daily maximum temperature at d day in this event; T_{25p}, and T_{75p} are the 25th and 75th percentile of the T_{max} in the warm season, respectively.

CDHWs are identified when a heatwave coincides with a monthly drought event[24]. We also calculate the CDHW_r to represent CDHW characteristics based on the ratio of the total number of CDHW and heatwave events occurring at any given location[24]. The severity of CDHW is estimated as the product of the daily standardized values of T_{max} and the daily TWS-DSI (the value is determined as same with the monthly TWS-DSI for each month) in the CDHW event. Thus, the severity for an CDHW (CDHW_s) is given as:

$$CDHW_s = \sum_{d=1}^{d=CDHW_D} \left(\left(-1 \times TWS\text{-}DSI_d \right) \times \left(\frac{T_{\max,d} - T_{25p}}{T_{75p} - T_{25p}} \right) \right) \quad ; CDHW_D \geq 3 \tag{5}$$

where $CDHW_D$ represents the duration of the coinciding days; $TWS\text{-}DSI_d$ is the TWS-DSI value at day *d*, which is consistent at a monthly scale.

Bivariate risk assessments of CDHW. We first quantify changes in the frequency, days, duration, severity (and CDHW_r) of droughts, heatwaves and CDHW from the historical period to the future period (2070-2099), respectively. Furthermore, to jointly understand the changes in both heatwave and drought severity under CDHW hazards, we analyse the shifts of bivariate return period by using non-stationary copulas, which are often used to describe the dependence between physical variables[56]. Here, we initially estimate the marginal distributions of HW_s and D_s of CDHW during the historical period by using six candidate distributions (i.e., Gamma, Normal, GEV, Weibull, Log-normal and inverse Gaussian) as candidates. Then we consider commonly used bivariate copula families (Gaussian copula, Student's t copula, and Archimedean copulas) to link the marginal distributions of historical HW_s and D_s. To reduce the uncertainty sourced from different marginal and joint distributions, only the best-fitting functions are used for fitting HW_s and D_s under future climates. We choose the Akaike information criterion to determine both the best-fitting marginal distributions and associated copulas[57], and employ the 'AND' definition of JRP to measure the bivariate hazards of CDHW, which is consistent with the approach of counting concurrent exceedances[58]. Therefore, the JRP is given as:

$$JRP = \frac{E}{1 - F_{HW} - F_{DR} + C(F_{HW}, F_{DR})} \tag{6}$$

where F_{HW} (F_{DR}) is the marginal cumulative distribution of HW_s (D_s), and $C(F_{HW}, F_{DR})$ represents the joint distribution of F_{HW} and F_{DR}; while the E denotes the average inter-arrival time between compound events.

Using copulas to model the dependence of heatwave and drought allows an assessment of the change in the likelihood of extreme (i.e., 50-year) CDHW. Therefore, the time-varying copula functions of HW_s and D_s are constructed by moving a 30-year window, with the aim to investigate the shifts of the bivariate CDHW hazard as well as the socioeconomic exposure to increasing risks under climate change. First, we estimate the quantiles of HW_s and D_s under a given JRP during the historical period (T_h, determined as the 50-year JRP in this study). As there are infinite points on the isoline of a given JRP, the likelihood of each event must be taken into consideration. Therefore, the most likely realization is optimized by achieving the maximum joint probability density[34,59]:

$$\begin{cases} (HW_s^*, D_s^*) = \arg\max \ f(HW, DR) = c(F_{HW}, F_{DR}) \cdot f_{HW} \cdot f_{DR} \\ c[F_{HW}, F_{DR}] = \dfrac{dC[F_{HW}, F_{DR}]}{d(F_{HW})d(F_{DR})} \end{cases} \tag{7}$$

where $c(F_{HW}, F_{DR})$ is the copula probability density function; f_{HW} and f_{DR} denote the probability density functions of F_{HW} and F_{DR}, respectively; and (HW_s^*, D_s^*) is the most likely realization under the given historical JRP (T_h).

After estimating the (HW_s^*, D_s^*) during the historical period by linking Eqs. (6)-(7), the 30-year period is used as a sliding time window (consistent with the length of the historical period), and the time-varying marginal distributions and copula functions are constructed moving from

2006 to 2099 at a 30-year window. After substituting (HW_s^*, D_s^*) into the time-varying distribution function of the k^{th} sliding window in the future period, an updated JRP $T_f(k)$ is calculated. If $T_f(k) < T_h$, it means that the bivariate CDHW risk in the k^{th} time window increases, and vice versa. As a result, the socioeconomic exposure arising from increasing bivariate risks can be measured by the following formula:

$$E_{pop} = \frac{I(T_h - T_f(k)) \cdot POP_k}{\sum_{k=N_1}^{k=N_2} POP_k} \times 100\% \tag{8}$$

$$E_{GDP} = \frac{I(T_h - T_f(k)) \cdot GDP_k}{\sum_{k=N_1}^{k=N_2} GDP_k} \times 100\% \tag{9}$$

where E_{pop} and E_{GDP} denote the population and GDP exposures to increasing bivariate CDHW risks, respectively; POP_k and GDP_k denote the population and GDP in the k^{th} year; $I(\bullet)$is indication function, when $T_h - T_f(k) > 0$, I=1; if conversely, I=0; N_1 and N_2 denote the starting and ending year of the study period, respectively.

Uncertainty decomposition using multivariate ANOVA method. To project future changes in the JRP of CDHW, we implemented 96 scenarios in the impact modelling chain, which consists of three RCPs, four GCMs and eight THMs under ISIMIP2b. In this study, the overall uncertainty is estimated by the variance of the average JRP during the future period, and then it is decomposed into the contributions from different sources using the multivariate ANOVA method[60]. The change in the climatic indicator $\Delta y_{i,j,k}$ (i.e., updated JRP of the historical 50-year CDHW in this study) is assumed to follow the following model:

$$\Delta y_{i,j,k} = \mu + R_i + G_j + H_k + I_{i,j,k} \tag{10}$$

where μ represents the mean change of the model ensemble of the climatic indicator; R_i, G_j and H_k represent the effects on the climatic indicator of the i^{th} RCP, j^{th} GCM, and k^{th} THM, respectively; and $I_{i,j,k}$ represents the sum of the effects due to the interaction between different sources.

Based on the multivariate ANOVA method, the total variance (overall uncertainty, VT) can be decomposed into contributions from different sources as follows:

$$VT = VR + VG + VH + VI_{RG} + VI_{RH} + VI_{RGH} \tag{11}$$

where VR, VG, VH present the variance contributed by the effects of RCPs, GCMs and THMs, respectively; VI_{RG}, VI_{RH} and VI_{RGH} represent the variance from interaction effects between RCP-GCM, RCP-THM and RCP-GCM-THM, respectively. By dividing the variance from different sources by the total variance, the fractional contributions of different sources to the overall uncertainty are obtained. We also employ the multivariate ANOVA method to quantify the contribution of uncertainty sources in the CMIP6-based projections.

References

1. Zhang, P. et al. Abrupt shift to hotter and drier climate over inner East Asia beyond the tipping point. *Science* **370**, 6520 (2020).
2. Jaeger, W.K. et al. Scope and limitations of drought management within complex human-natural systems. *Nat. Sustain*. **2**, 710-717 (2019).
3. Lim, E.P. et al. Australian hot and dry extremes induced by weakenings of the stratospheric polar vortex. *Nat. Geosci*. **12**, 896-901 (2019).
4. Bevacqua, E. et al. Precipitation trends determine future occurrences of compound hot–dry events. *Nat. Clim. Change* **12**, 350-355 (2022).
5. Dirmeyer, P. A., Jin, Y., Singh, B. & Yan, X. Evolving land-atmosphere interactions over North America from CMIP5 simulations. *J. Clim.* **26**, 7313-7327 (2013).
6. Alizadeh, M. R. et al. A century of observations reveals increasing likelihood of continental-scale compound dry-hot extremes. *Sci. Adv*. **6**, eaaz4571 (2020).
7. Reichstein, M. et al. Climate extremes and the carbon cycle. *Nature* **500**, 287-295 (2013).
8. Gampe, D. et al. Increasing impact of warm droughts on northern ecosystem productivity over recent decades. *Nat. Clim. Change* **11**, 772-779 (2021).
9. Williams, A. P. et al. Temperature as a potent driver of regional forest drought stress and tree mortality. *Nat. Clim. Change* **3**, 292-297 (2013).
10. Anderegg, W. R. et al. Pervasive drought legacies in forest ecosystems and their implications for carbon cycle models. *Science* **349**, 528-532 (2015).

11. Zampieri, M., Ceglar, A., Dentener, F. & Toreti, A. Wheat yield loss attributable to heat waves, drought and water excess at the global, national and subnational scales. *Environ. Res. Lett*. **12**, 064008 (2017).
12. Guerreiro, S. B. et al. Future heat-waves, droughts and floods in 571 European cities. *Environ. Res. Lett.* **13**, 034009 (2018).
13. Keenan, T. F. et al. A constraint on historic growth in global photosynthesis due to increasing CO2. *Nature* **600**, 253-258 (2021).
14. Noon, M. L. et al. Mapping the irrecoverable carbon in Earth's ecosystems. *Nat. Sustain*. **5**, 37-46 (2022).
15. Ciais, P. et al. Europe-wide reduction in primary productivity caused by the heat and drought in 2003. *Nature* **437**, 529-533 (2005).
16. Ruehr, N. K., Grote, R., Mayr, S. & Arneth, A. Beyond the extreme: recovery of carbon and water relations in woody plants following heat and drought stress. *Tree Physiol*. **39**, 1285-1299 (2019).
17. Lobell, D. B., Deines, J. M. & Tommaso, S. D. Changes in the drought sensitivity of US maize yields. *Nat. Food* **1**, 729-735 (2020).
18. Schwalm, C. R. et al. Global patterns of drought recovery. *Nature* **548**, 202-205 (2017).
19. Zhou, S., Zhang, Y., Williams, A. P. & Gentine, P. Projected increases in intensity, frequency, and terrestrial carbon costs of compound drought and aridity events. *Sci. Adv*. **5**, eaau5740 (2019).
20. Mazdiyasni, O. & AghaKouchak, A. Substantial increase in concurrent droughts and heatwaves in the United States. *Proc. Natl. Acad. Sci. USA* **112**, 11484-11489 (2015).
21. Zscheischler, J. et al. A typology of compound weather and climate events. *Nat. Rev. Earth Environ.* **1**, 333-347 (2020).
22. Naumann, G. et al. Increased economic drought impacts in Europe with anthropogenic warming. *Nat. Clim. Change* **11**, 485-491 (2021).
23. Satoh, Y. et al. A quantitative evaluation of the issue of drought definition: a source of disagreement in future drought assessments. *Environ. Res. Lett.* **16**, 104001 (2021).
24. Mukherjee, S. & Mishra, A. K. Increase in compound drought and heatwaves in a warming world. *Geophys. Res. Lett.* **48**, e2020GL090617. (2021).
25. Zhao, M. et al. Ecological restoration impact on total terrestrial water storage. *Nat. Sustain*. **4**, 56-62 (2021).
26. Pokhrel, Y. et al. Global terrestrial water storage and drought severity under climate change. *Nat. Clim. Change* **11**, 226-233 (2021).
27. Zhang, Y., Joiner, J., Alemohammad, S.H., Zhou, S. & Gentine, P. A global spatially contiguous solar-induced fluorescence (CSIF) dataset using neural networks. *Biogeosci*. **15**, 5779-5800 (2018).
28. Zhang, Y. et al. A global moderate resolution dataset of gross primary production of vegetation for 2000–2016. *Sci. Data* **4**, 170165 (2017).
29. Zhou, S. et al. Land-atmosphere feedbacks exacerbate concurrent soil drought and atmospheric aridity. *Proc. Natl Acad. Sci. USA* **116**, 18848-18853 (2019).
30. Lobell, D. B. et al. The critical role of extreme heat for maize production in the United States. *Nat. Clim. Change* **3**, 497-501 (2013).
31. Drake, J. E. et al. A common thermal niche among geographically diverse populations of the widely distributed tree species Eucalyptus tereticornis: No evidence for adaptation to climate-of-origin. *Glob. Chang. Biol*. **23**, 5069-5082 (2017).

32. Novick, K. A. et al. The increasing importance of atmospheric demand for ecosystem water and carbon fluxes. *Nat. Clim. Change* **6**, 1023-1027 (2016).
33. Nemani, R. R. et al. Climate-driven increases in global terrestrial net primary production from 1982 to 1999. *Science* **300**, 1560-1563 (2003).
34. Yin, J. et al. Projection of droughts and their socioeconomic exposures based on terrestrial water storage anomaly over China. *Sci. China Earth Sci.* **65**, 1772-1787 (2022).
35. Campbell, J. E. et al. Large historical growth in global terrestrial gross primary production. *Nature* **544**, 84-87 (2017).
36. Wang, X. et al. Emergent constraint on crop yield response to warmer temperature from field experiments. *Nat. Sustain.* **3**, 908-916 (2020).
37. Allen, C. D., Breshears, D. D. & McDowell, N. G. On underestimation of global vulnerability to tree mortality and forest die-off from hotter drought in the Anthropocene. *Ecosphere* **6**, 129 (2015).
38. Rodrigues, R. R. & Woollings, T. Impact of atmospheric blocking on South America in austral summer. *J. Clim*. **30**, 1821-1837 (2017).
39. Büntgen, U. et al. Recent European drought extremes beyond Common Era background variability. *Nat. Geosci*. **14**, 190-196 (2021).
40. Schumacher, D.L. et al. Amplification of mega-heatwaves through heat torrents fuelled by upwind drought. *Nat. Geosci*. **12**, 712-717 (2019).
41. Hallegatte, S. et al. Poverty and climate change: introduction. *Environ. Dev. Econ*. **23**, 217–233 (2018).
42. Fankhauser S. & McDermott T.K.J. Understanding the adaptation deficit: Why are poor countries more vulnerable to climate events than rich countries?. *Global Environ. Chang*. **27**, 9-18 (2014).
43. Burke, M., Hsiang, S. & Miguel, E. Global non-linear effect of temperature on economic production. *Nature* **527**, 235-239 (2015).
44. Elkouk, A. et al. Implications of changes in climate and human development on 21st-century global drought risk. *J. Environ. Manage*. **317**, 115378 (2022).
45. Lange, S. Bias correction of surface downwelling longwave and shortwave radiation for the EWEMBI dataset. *Earth Syst. Dyn*. **9**, 627-645 (2018).
46. Lange, S. Trend-preserving bias adjustment and statistical downscaling with ISIMIP3BASD (v1. 0). *Geosci. Model Dev*. **12**, 3055-3070 (2019).
47. Humphrey, V. & Gudmundsson, L. Grace-rec: a reconstruction of climate-driven water storage changes over the last century. *Earth Syst. Sci. Data* **11**, 1153-1170. (2019).
48. Reichstein, M. et al. On the separation of net ecosystem exchange into assimilation and ecosystem respiration: Review and improved algorithm. *Glob. Chang. Biol.* **11**, 1424-1439 (2005).
49. Pastorello G. et al. The FLUXNET2015 dataset and the ONEFlux processing pipeline for eddy covariance data. *Sci. Data* **7**, 225 (2020).
50. Kummu, M. et al. Gridded global datasets for Gross Domestic Product and Human Development Index over 1990–2015. *Sci. Data* **5**, 180004 (2018).
51. Jing, C. et al. Population, urbanization and economic scenarios over the Belt and Road region under the Shared Socioeconomic Pathways. *J. Geogr. Sci*. **30**, 68-84 (2020).
52. Koutsoyiannis, D. Clausius-Clapeyron equation and saturation vapor pressure: simple theory reconciled with practice. *Eur. J. Phys*. **33**, 295-305 (2012).

53. Simmons, A. J., Untch, A., Jakob, C., Kallberg, P. & Unden P. Stratospheric water vapor and tropical tropopause temperatures in ECMWF analyses and multi-year simulations. *Q. J. R. Meteorol. Soc.* **125**, 353-386 (1999).
54. Zhao, M., Velicogna, I. & Kimball, J. S. Satellite observations of regional drought severity in the continental United States using GRACE-based terrestrial water storage changes. *J. Clim*. **30**, 6297-6308 (2017).
55. Keellings, D. & Waylen, P. Increased risk of heat waves in Florida: Characterizing changes in bivariate heat wave risk using extreme value analysis. *Appl. Geogr*. **46**, 90-97. (2014).
56. Yin, J. et al. Global increases in lethal compound heat stress: hydrological drought hazards under climate change. *Geophys. Res. Lett*. **49**, e2022GL100880. (2022).
57. Akaike, H. A new look at the statistical model identification. *IEEE Trans. Automat. Contr*. **19**, 716-723 (1974).
58. Zscheischler, J. & Seneviratne, S. I. Dependence of drivers affects risks associated with compound events. *Sci. Adv*. **3**, e1700263 (2017).
59. Salvadori, G. et al. A multivariate copula-based framework for dealing with hazard scenarios and failure Probabilities. *Water Resour. Res*. **52**, 3701-3721 (2016).
60. Chegwidden, O. S. et al. How do modeling decisions affect the spread among hydrologic climate change projections? Exploring a large ensemble of simulations across a diversity of hydroclimates. *Earth's Future* **7**, 623-637 (2019).

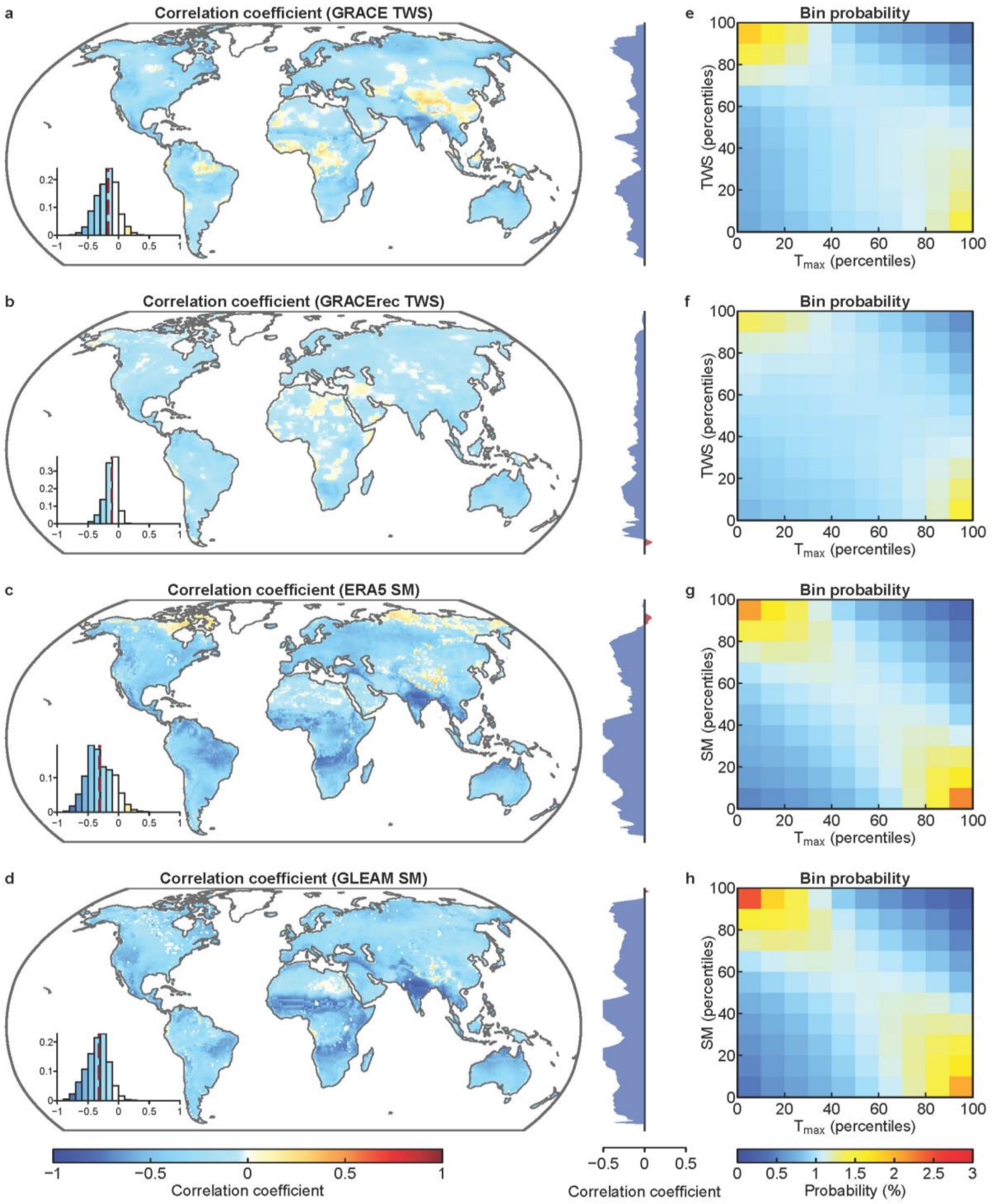

Extended Data Fig. 1 | Relationship between daily maximum near-surface temperature (T_{max}) and terrestrial water storage (TWS) or root-zone soil moisture (SM) during 2002-2020. a-d, Pearson's correlation coefficient between: monthly GRACE/GRACE-FO ensemble mean TWS and ERA5 T_{max} (**a**), monthly reconstructed TWS and T_{max} from Berkeley Earth Surface Temperatures (**b**), daily ERA5 SM and T_{max} (**c**), daily GLEAM SM and ERA5 T_{max} (**d**). Insets in **a-d** show the histogram of the correlation coefficient, with the dashed vertical line representing the median value. The graph on the right of each panel shows the latitudinal median. **e-h**, Mean probability of each percentile bin across all land grid cells (excluding Greenland and Antarctica in all analyses).

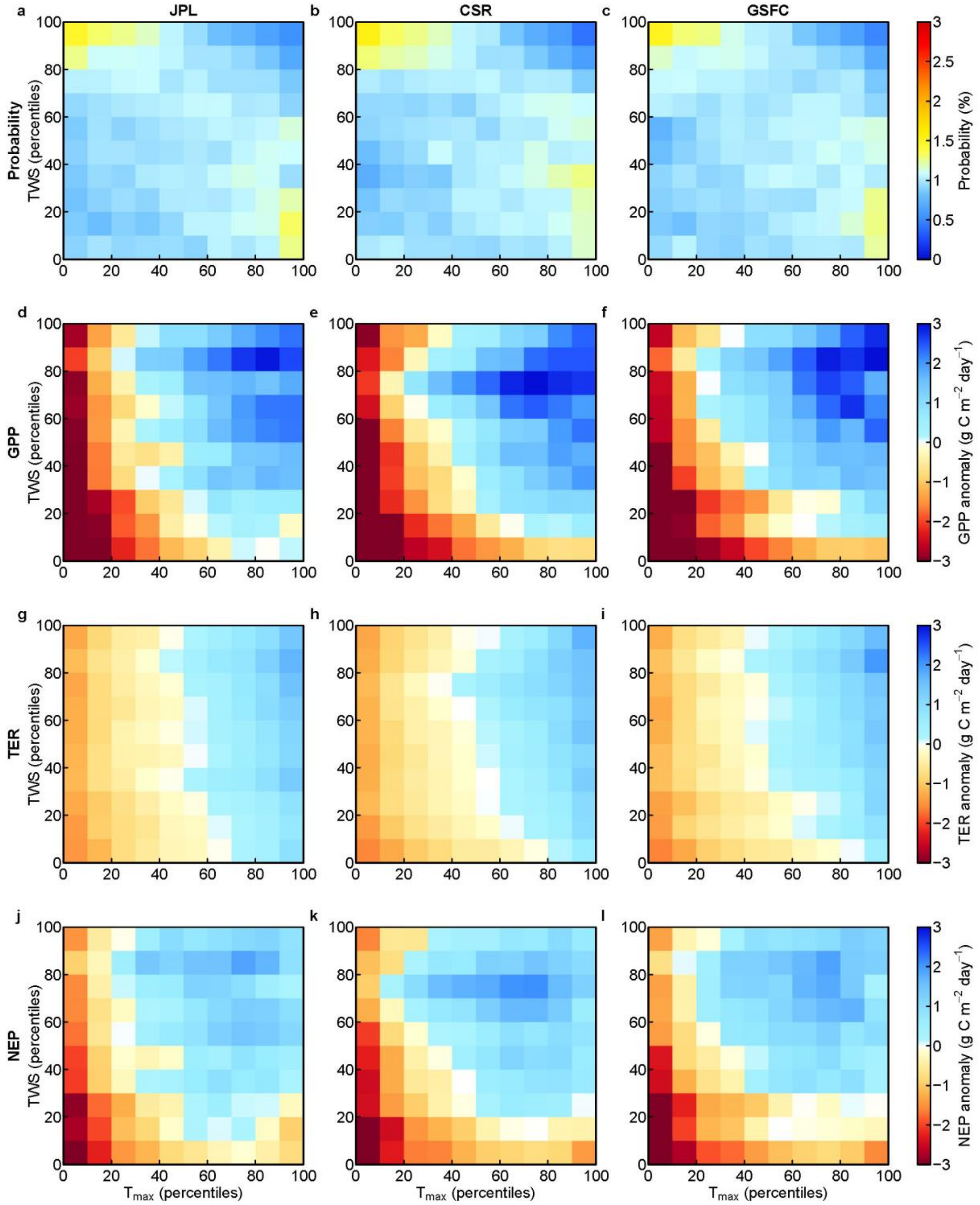

Extended Data Fig. 2 | Coupling of T_{max} and monthly TWS from the three GRACE/GRACE-FO solutions dataset and their impacts on terrestrial carbon uptake. a-c, Probability of each percentile bin of T_{max} and monthly TWS across 73 flux tower sites. **d-f**, Mean anomalies of GPP for each percentile bin of T_{max} and TWS. **g-i**, Mean anomalies of TER for each percentile bin of T_{max} and TWS. **j-l**, Mean anomalies of NEP for each percentile bin of T_{max} and TWS. The three columns represent the GRACE/GRACE-FO TWS data produced from JPL, CSR and GSFC, respectively. At each site, anomalies of GPP, TER, and NEP are calculated as the difference between the daily values in extreme events and the mean daily values in the warm season (defined as days when running 7-day mean temperatures are higher than the 60th percentile of daily temperature for the site).

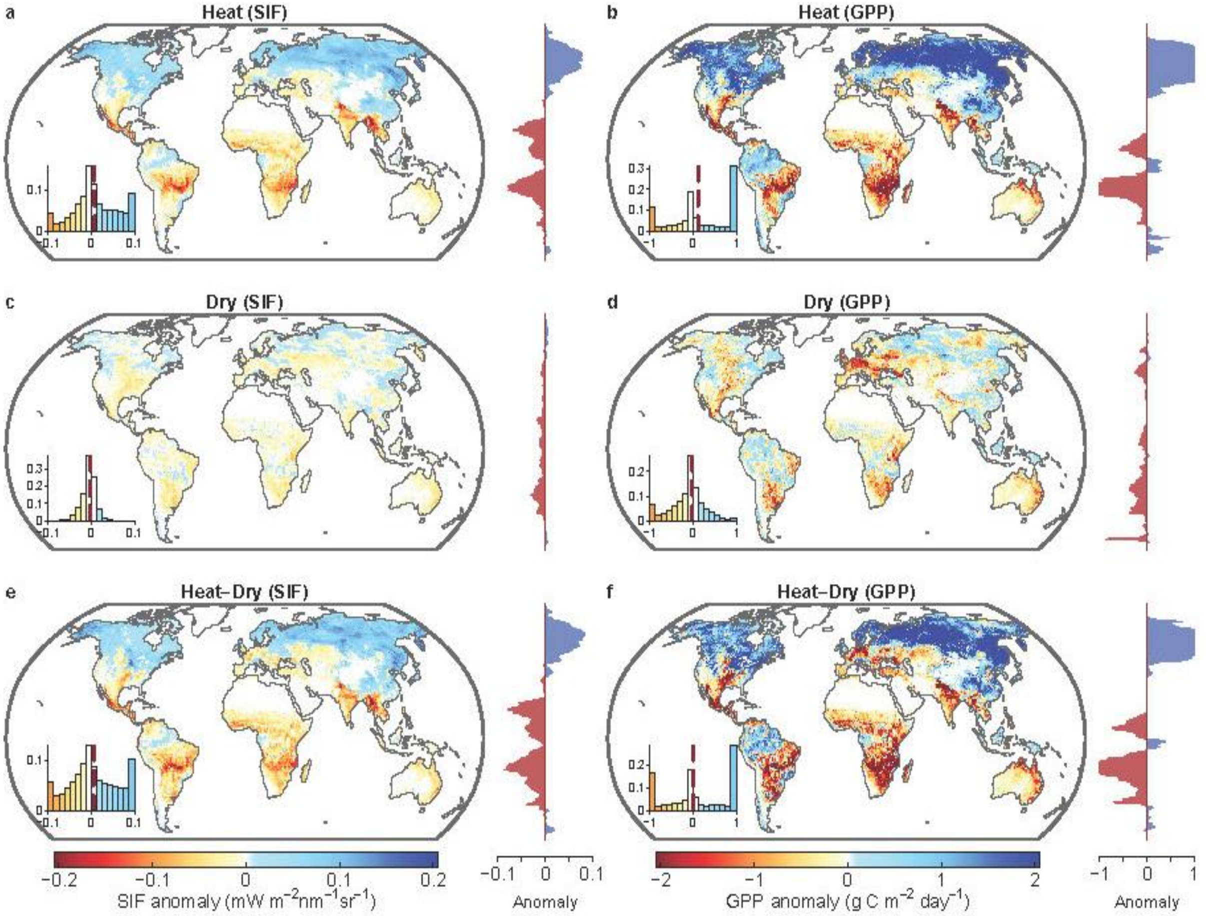

Extended Data Fig. 3 | Anomalies of SIF and GPP during extreme climatic events. **a-b**, Anomalies of SIF (**a**) and GPP (**b**) during extreme heat events. **c-d**, Anomalies of SIF (**c**) and GPP (**d**) during extreme dry events. **e-f**, Anomalies of SIF (**e**) and GPP (**f**) in concurrent heat and dry conditions. At each grid, anomalies of SIF (GPP) are calculated as the difference between the 4-day (8-day) values in extreme events and the mean 4-day (8-day) values in the warm season. Dry conditions are identified using GRACE/GRACE-FO ensemble mean TWS data, and the heat conditions are identified by ERA5 T_{max}. Insets show the histogram of the anomalies, with the dashed vertical line representing the median value. The graph on the right shows the latitudinal median value.

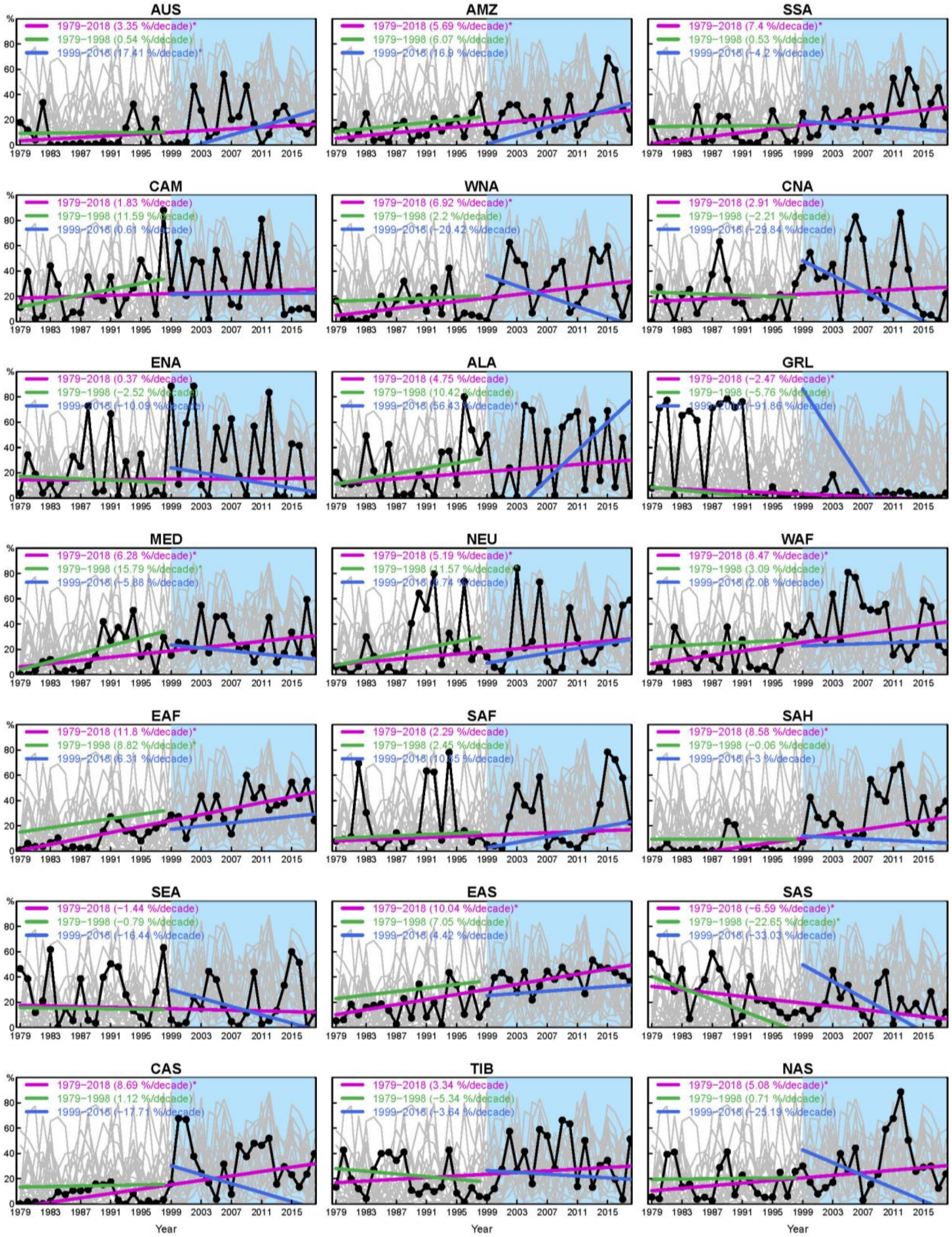

Extended Data Fig. 4 | Temporal dynamics of the GDP exposures to CDHW in 21 Giorgi climate regions. Each panel has a cluster of 21 grey lines, which show the ensemble of the regional GDP exposures in all regions. The black line in each figure represents the exposure value in each region, and the color lines represent trends of GDP exposures during recent, past and entire periods. The droughts are identified by reconstructed TWS data, and the heatwaves are detected by using T_{max} from the BEST dataset. The * indicates the trend is significant ($p<0.05$) detected by Mann-Kendall test.

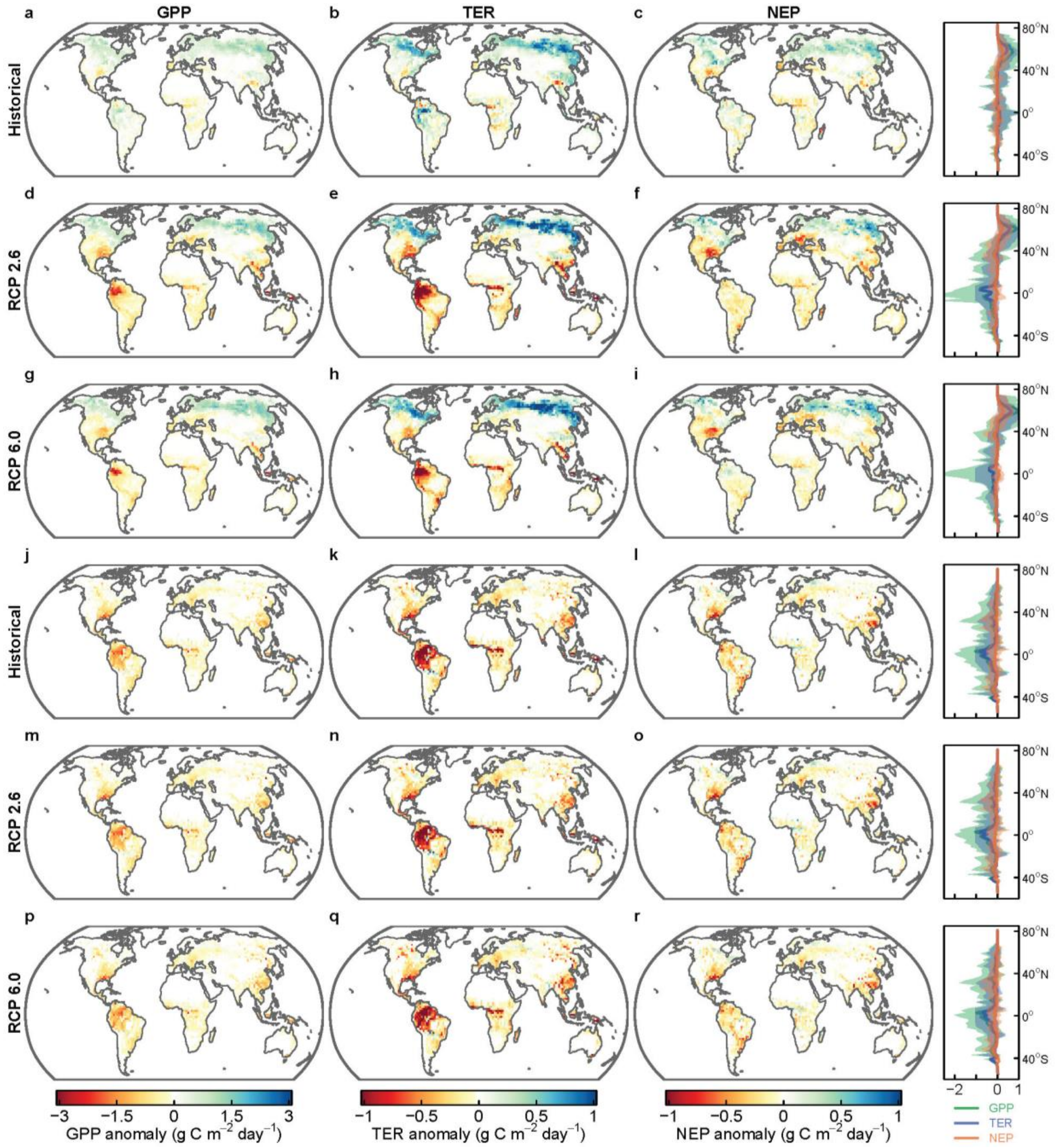

Extended Data Fig. 5 | Anomalies of GPP, TER and NEP due to extreme heat or drought conditions in the GFDL-CLM4.5 model. a-i, Anomalies of carbon fluxes in the historical period (**a-c**), RCP 2.6 (**d-f**) and RCP 6.0 (**g-i**) due to extreme heat conditions (monthly T_{max} above the 90th percentile). **j-r**, Anomalies of carbon fluxes in the historical period (**j-l**), RCP2.6 (**m-o**) and RCP6.0 (**p-r**) due to droughts (TWS-DSI< -0.8). The graph on the right shows the latitudinal median and 90% confidence interval. The TWS and carbon fluxes are projected by CLM4.5 model with bias-corrected GFDL-GCM2M outputs.

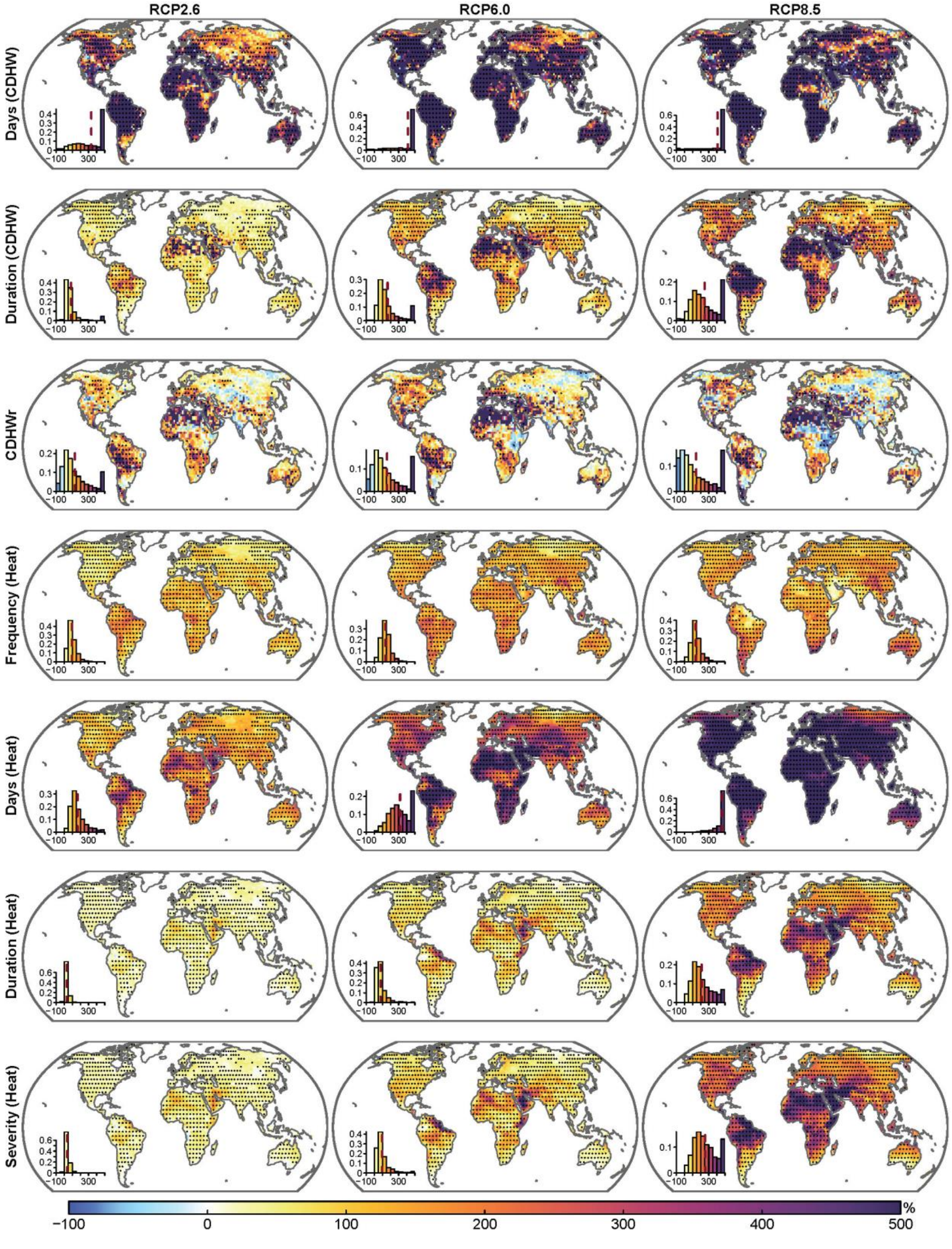

Extended Data Fig. 6 | Future changes in characteristics of CDHW and heatwaves. Insets in each figure show the histogram of the relative change percentages, with the dashed vertical line representing the mean value. Stippling denotes regions where the sign of the relative changes is consistent with the sign of the multi-model means (as shown in the figure) in at least 80% of GCM-THM models. These results are derived from the ISIMIP2b multiple impacts model ensemble.

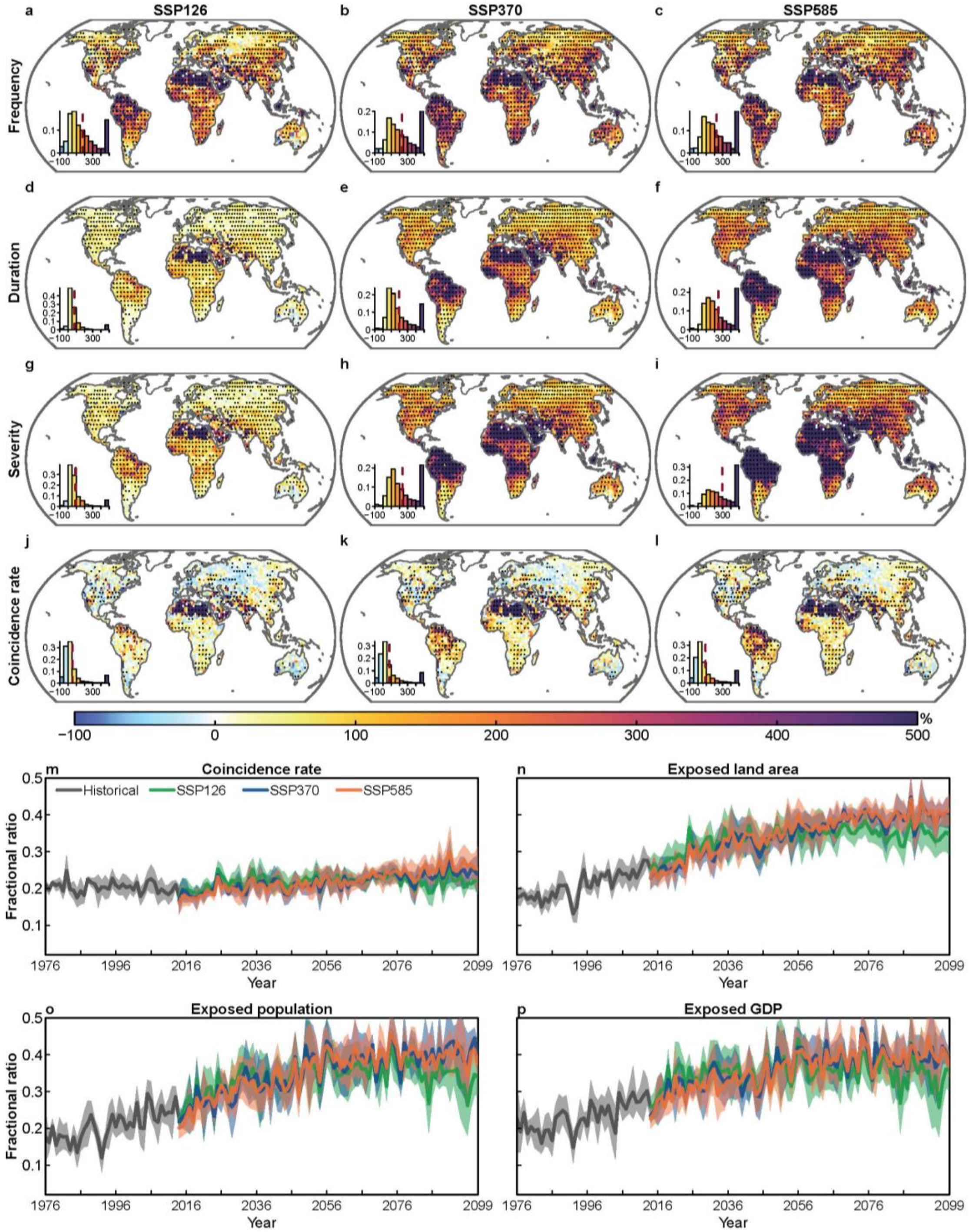

Extended Data Fig. 7 | Future changes in the characteristics of CDHW and socioeconomic exposure to CDHW under CMIP6. a-l, Relative changes in the frequency (**a-c**), average duration (**d-f**), average severity (**g-i**) and coincidence rate (**j-l**) of CDHW from the historical to the future periods. **m-p**, Temporal dynamics of the global average coincidence rate (**m**), exposed land area (**n**), exposed population (**o**) and exposed GDP (**p**). Insets in **a-l** show the histogram of the relative change percentages, with the dashed vertical line representing the mean value. Stippling in **a-l** denotes regions where the sign of the relative changes is consistent with the sign of the multi-model means (as shown in the figure) in at least 80% of GCMs. In **m-p**, the shading represents ±1 standard deviation, and only the historical exposures linking to SSP126 TWS data are presented. For projecting CDHW, the TWS is simulated by driving H08 forced by five bias-corrected GCMs under CMIP6.

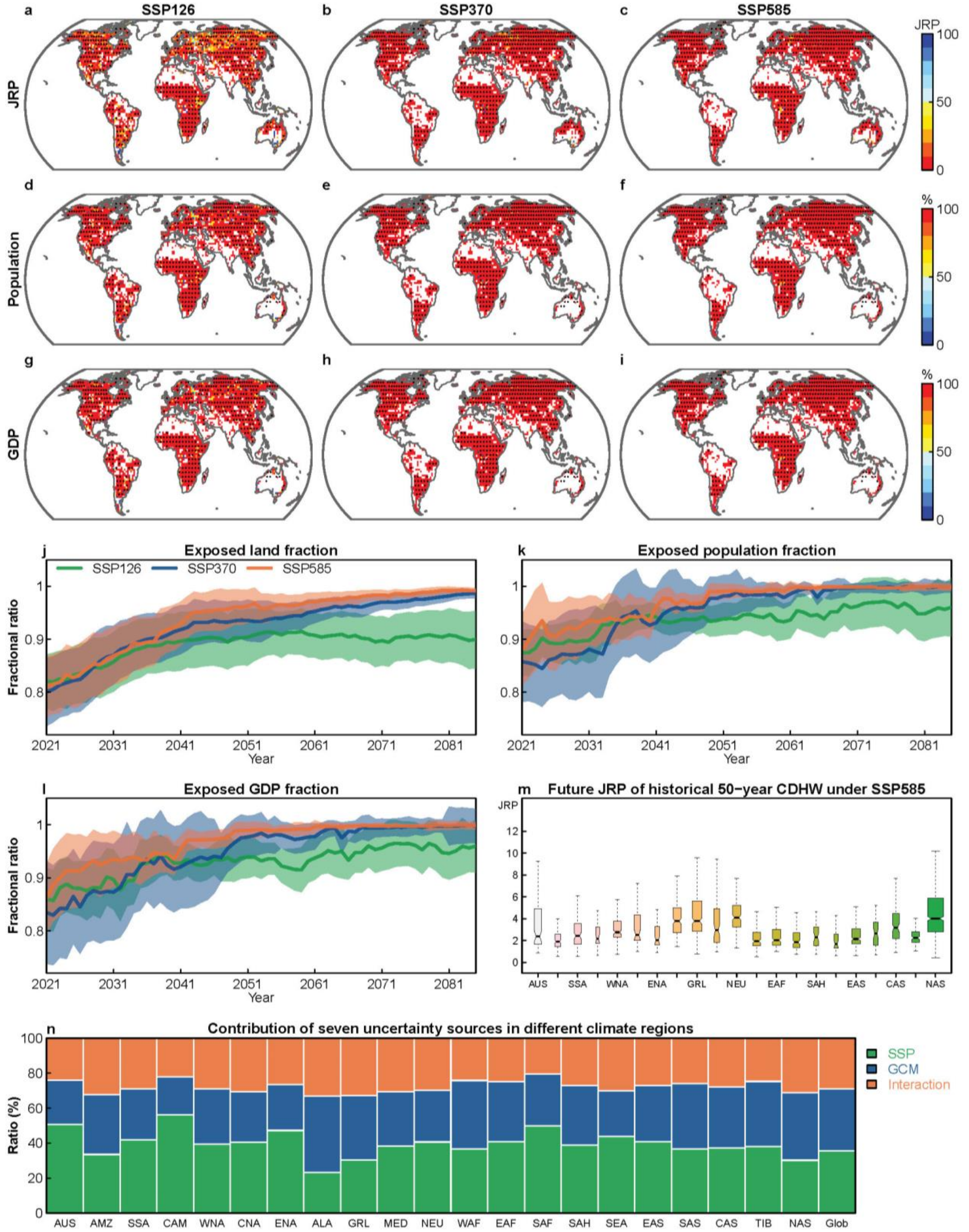

Extended Data Fig. 8 | Projected JRP of historical 50-year bivariate CDHW and socioeconomic exposure under CMIP6. a-c, Average JRP in the future period under a non-stationary bivariate framework. **d-i**, Population (**d-f**) and GDP (**g-i**) exposure due to increasing risk of bivariate CDHW in the future period. j-l, Temporal dynamics of the global average exposed land area (**j**), population (**k**) and GDP (**l**) due to increasing CDHW risk; the solid curve and shading indicate multi-model mean ±SD. **m**, Boxplot of updated JRP of the historical 50-year CDHW in different Giorgi climate regions under SSP585; the centre line indicates median value, and the box bounds (whiskers) indicate 25th/75th percentile (min/max) values. **n**, Average contribution ratios of seven uncertainty sources in different Giorgi climate regions and in the global landmass (Glob). Stippling in **a-i** denotes regions where the sign of the JRP is consistent with the sign of the multi-model means (as shown in the figure) in at least 80% of GCMs. For projecting CDHW, the TWS is simulated by driving H08 forced by five bias-corrected GCMs under CMIP6.

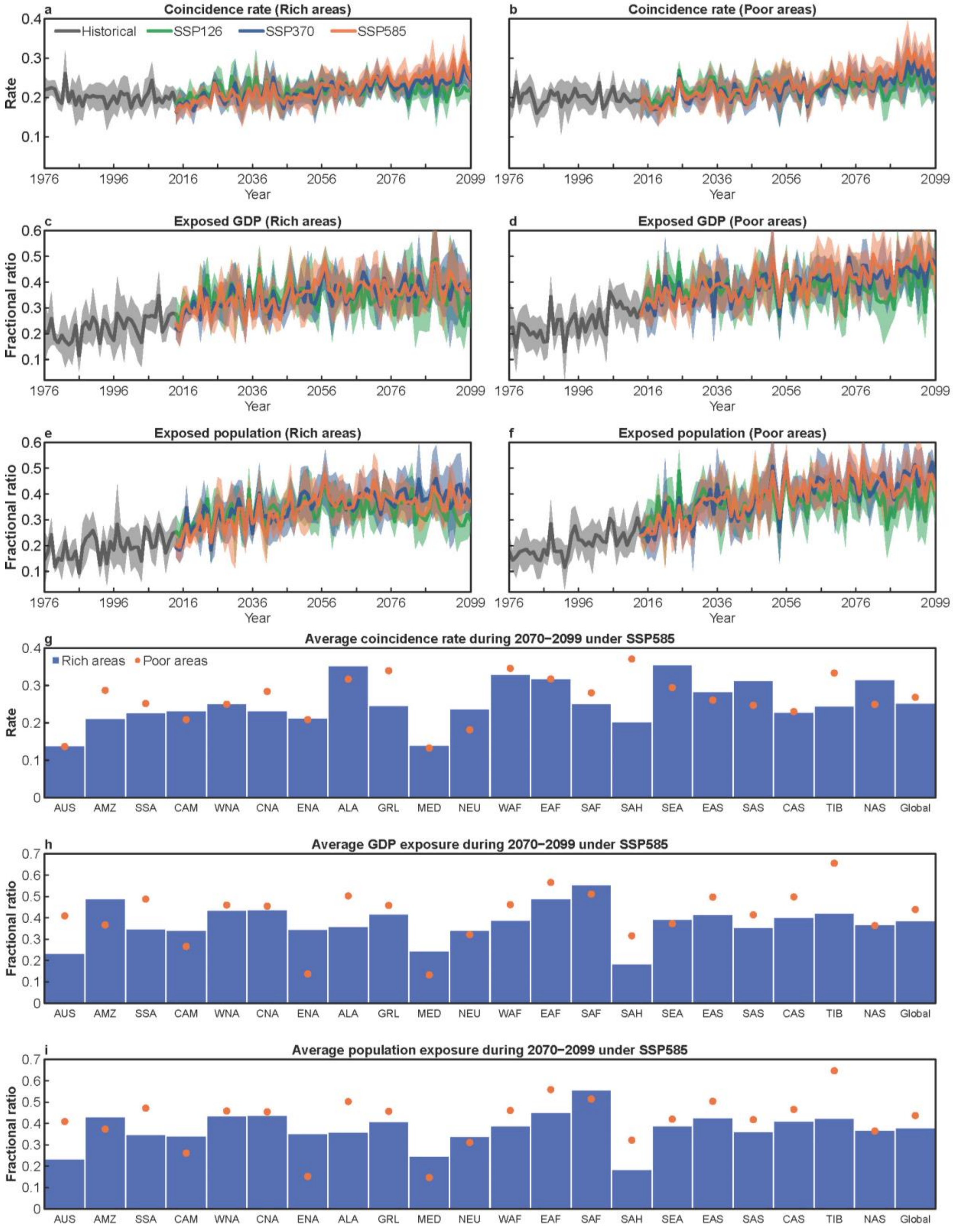

Extended Data Fig. 9 | CDHW coincidence rate and socioeconomic exposures to CDHW in rich versus poor areas. a-f, Temporal dynamics of the global average coincidence rate (**a-b**), and exposed GDP fraction (**c-d**) and population fraction (**e-f**) to CDHW. **g-i**, Average coincidence rate (**g**), GDP exposure fraction (**h**) and population exposure fraction (**i**) during 2070-2099 in different Giorgi climate regions under SSP585. In **a-f**, the shading represents ±1 standard deviation, and only the historical exposures linking to SSP126 TWS data are presented. For projecting CDHW, the TWS is simulated by driving H08 forced by five bias-corrected GCMs under CMIP6. Rich (poor) areas are identified where the 2015-year GDP per capita exceeds (is below) the 80th (20th) percentile values in different regions.

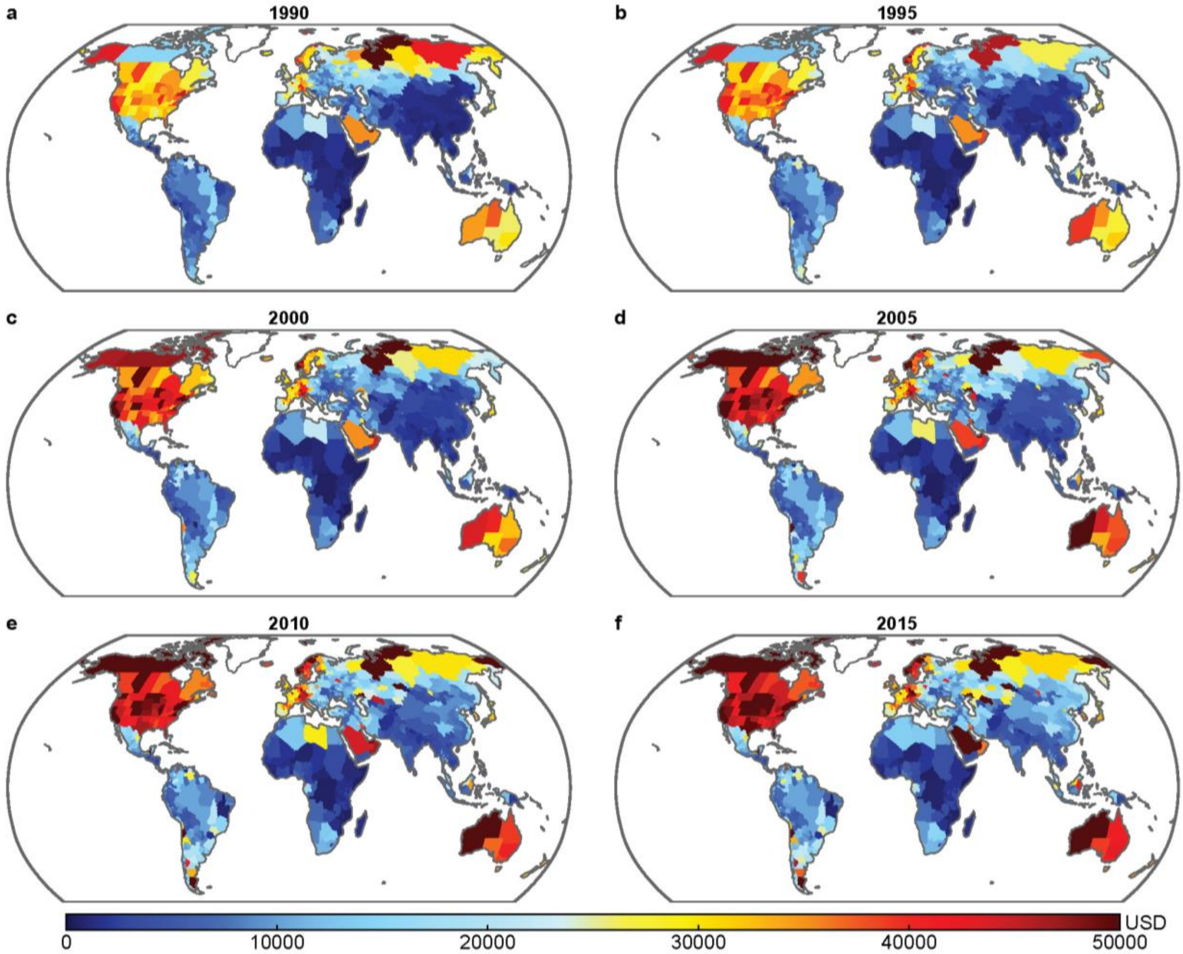

Extended Data Fig. 10 | Gridded Gross Domestic Product (GDP) per capita (purchasing power parity) in constant 2011 international US dollars (USD) for six typical years during 1990–2015. a-f, GDP per capita in year of 1990 (**a**), 1995 (**b**), 2000 (**c**), 2005 (**d**), 2010 (**e**) and 2015 (**f**).